Acta Astronautica 138 (2017) 512–529

Contents lists available at ScienceDirect

Acta Astronautica

journal homepage: www.elsevier.com/locate/actaastro

Modeling of Active Tether System concepts for planetary exploration

Marco B. Quadrelli *, Masahiro Ono, Abhinandan Jain

Mobility and Robotic Systems Section, Autonomous Systems Division, Jet Propulsion Laboratory, California Institute of Technology, 4800 Oak Grove Drive, Pasadena, CA 91109, United States

A B S T R A C T

This paper summarizes an approach for modeling, simulation, and control of tethered systems in which the tether is actively controlled. Various aspects of the system model are described, including tether dynamics, end-effector dynamics, contact interaction and the model of the active tether material. We consider three scenarios: a tether made of an electrically switchable material for small body sampling, a tether for close-proximity operations such as capture and grappling, and a tether harpooning to a small body for sample capture, fly-by, rendezvous, and/or landing.

1. Introduction

This paper summarizes an approach for modeling, simulation, and control of tethered systems in which the tether is actively controlled. Various aspects of the system model are described, including tether dynamics, end-effector dynamics, contact interaction and the model of the active tether material. We consider three scenarios (Fig. 1): a tether made of an electrically switchable material for small body sampling, a tether for close-proximity operations such as capture and grappling, and a tether harpooning to a small body for sample capture or planetary fly-by.

Extreme planetary environments represent the next frontier for in situ robotic space exploration. Missions for exploration would be followed by robotic missions for exploitation, and by human missions. All these missions would have one common problem: highly irregular topography, heterogeneous surface properties (soft, hard), harsh, extreme environments, where temperature, radiation, and other factors make the missions inconceivable at present. Also, asset delivery and sample capture and return could be at the heart of several emerging potential missions to small bodies, such as asteroids and comets, and to the surface of large bodies, such as Titan. Furthermore, the diverse geologic sites would require versatile in situ science that can adapt to the local geology and environmental conditions. An Active Tether System (ATS) would show much promise to enable new types of mission concepts with lower risk sampling operations (being far away from the surface), higher rate of science data quality and return (samples with stratigraphy, sub-surface samples), and much more agility (sampling operations can be repeated multiple times at multiple locations without landing). In a multistage architecture, the ATS would become highly scalable, and would represent an advantage over existing asset deployment and potential sample capture mission operations because it would have the potential of further decoupling the end-effector operation from the spacecraft operation during the target interaction phase, thus enabling many new mission concepts. An ATS is different than an electrodynamic tether system as typically considered in space propulsion in that the ATS uses coupling between electromagnetism and mechanics to make the tether into an intelligent material system. One example of application could be the following: imagine approaching an asteroid and being able to reach the surface to deliver an asset or to collect a sample without ever having to land. By phase-transitioning its material characteristics in a multi-segmented boom, a long appendage (up to a few hundred meters long) would change its shape and its compliance actively to conform to any surface irregularity in any body of the Solar System. By eliminating complex proximity operations near the surface, this intelligent system could become the new way to interact at-a-distance with primitive bodies and potentially bring pristine soil samples back to Earth. We now describe the three scenarios considered in this paper.

Phase-transition tether: In this scenario, we investigate the modeling aspects of a tether system, which, through changing equilibrium phases in the material, is able to change its compliance in response to different external stimuli and collects a sample from the surface of a planetary body (Fig. 2). The paper approaches this complex problem sequentially. The first step is the static and dynamic characterization of the component behavior of an ATS element. Some phase-transitioning materials that are considered are piezoelectric materials, electro-rheological materials, electro-active polymers, photo-strictive and magneto-strictive materials. The second step is to investigate the system-level behavior under closed loop control, which is dependent on the scenario of application, i.e. the large scale dynamics and control aspects with an eye to performance of

* Corresponding author.
E-mail address: marco.b.quadrelli@jpl.nasa.gov (M.B. Quadrelli).

http://dx.doi.org/10.1016/j.actaastro.2016.11.010
Received 16 July 2016; Accepted 4 November 2016
Available online 12 November 2016
0094-5765/© 2016 IAA. Published by Elsevier Ltd. All rights reserved.

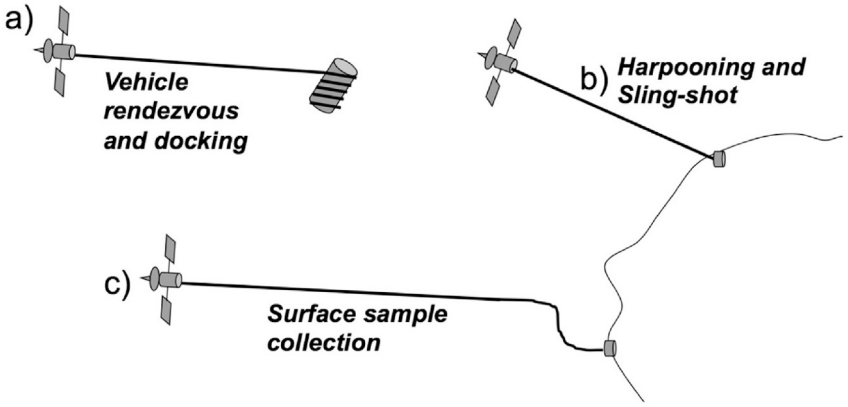

Fig. 1. The three cases considered in this paper for an active tether: (a) vehicle rendezvous and docking; (b) harpooning and sling-shot from a small body; (c) surface sample collection.

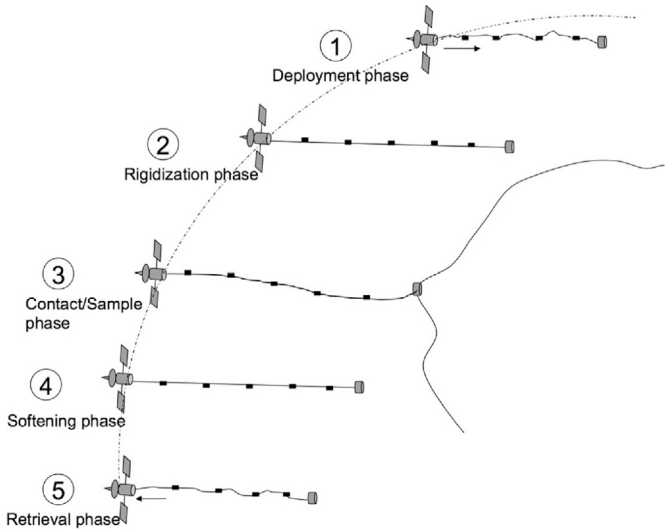

Fig. 2. Active tether used for adaptive small body sampling.

the space system in a relevant mission context. To achieve the full potential of distributed actuation, it is necessary to develop models that characterize the hysteretic nonlinearities inherent in the constituent materials, as well a distributed sensing methodology. We have investigated models that quantify the nonlinearities and hysteresis inherent to phase transition, each in formulations suitable for subsequent control design. These models involve first-order, nonlinear ordinary differential equations and require few parameters that are readily identifiable from measurements, hence we have selected to use these differential models in our analysis. To investigate the implications of using this concept, a multibody dynamics simulation of the system behavior of the entire vehicle during sample captures has been developed and tested in a simulation environment.

Harpooning and sling-shot tether: NASA is interested in designing a spacecraft capable of visiting a comet, performing experiments, and then returning safely. Certain periods of this mission would require a spacecraft to remain stationary relative to the NEO (Fig. 3, taken from [28]). Such situations would require an anchoring mechanism that is compact, easy to deploy and upon mission completion, easily removed. The design philosophy used in the project relies on the simulation capability of a multibody dynamics physics engine. On Earth it is difficult to create low gravity conditions and testing in low gravity environments, whether artificial or in space is costly and therefore not feasible. Through simulation, gravity can be controlled with great accuracy, making it ideally suited to analyze the problem at hand. Effective NEO exploration requires vehicle/astronaut anchoring due to extremely low gravity. Simulation and testing must be carried out with implications on system/mission design, system verification and validation, design of combined vehicle/human/robot teams, design of proximity operations such as landing, tethered operations, surface mobility, drilling, sub-surface sampling. The mission concept (Fig. 3, taken from [28]) would involve several phases: deployment (fire harpoon from 100 m+ from spacecraft (S/C)); sampler stabilization: (sampler would be stabilized during flight to surface via tension in tether); sampling: (sampler would impact, sample, close and eject sample canister); retrieval: (S/C would reel in tether while S/C thrusts, possibly with pendulum cancelation maneuver); sample measurement: (potentially compute from balance of forces given the spacecraft acceleration); canister capture: (pull back into chamber it was released from); canister transfer to SRC: (S/C arm would grasp canister and transfer to SRC). The benefits of this approach would primarily be low mission risk and capability of providing desirable science data. In regard to risk, the spacecraft would stay far from comet, and would never be on collision trajectory with comet. It would rely on a passive sampler, with the canister retrieval constrained to tether. The canister capture would be straightforward, and the canister transfer back to the spacecraft would also be straightforward. In terms of the desirable science, this approach would allow for sampling subsurface to 10 cm, maintaining stratigraphy, would allow multiple samples from different comet locations, and would minimize sample contamination. Once the spacecraft points the sampler at the target, then the sampler would simply be released toward the sample target. The tether spool would be on the sampler, and would be pulled out with constant tension, although another design option for active tether tension control would have the spool on the spacecraft instead. The tether tension would stabilize the sampler during flight to surface. Since the spacecraft could be at a stand-off distance, the tether could be long. It is assumed that a spacecraft would stand off from a cometary nucleus by hundreds or even thousands of meters, and fire a harpoon-type sample capture device into the comet. The simulation and experiments of the retrieving dynamics and control of tethered sampling systems for Small Body Exploration has been discussed in [17,18]. As an example of the tether sling-shot maneuver, we describe the Comet Hitchhiker concept (Fig. 4). The Comet Hitchhiker [21] concept would essentially perform momentum exchange with a target body using an extendable/retrievable tether. The momentum exchange would be performed in two ways: (i) to kill the relative velocity with the target and (ii) to accelerate the spacecraft in relative to the target. We call the former a *space hitchhike maneuver*, while the latter an *inverse space hitchhike maneuver*. The key idea of the Comet Hitchhiker concept is to use extendable/retrievable tether, which enables: (1) to control the spacecraft acceleration within a tolerable level, i.e. below the tensile strength of the tether and end-effector material, (2) to harvest the kinetic energy of the target body, and most importantly, (3) to change or completely kill the relative velocity with the target, hence enabling rendezvous and landing. First, the spacecraft harpoons a target as it

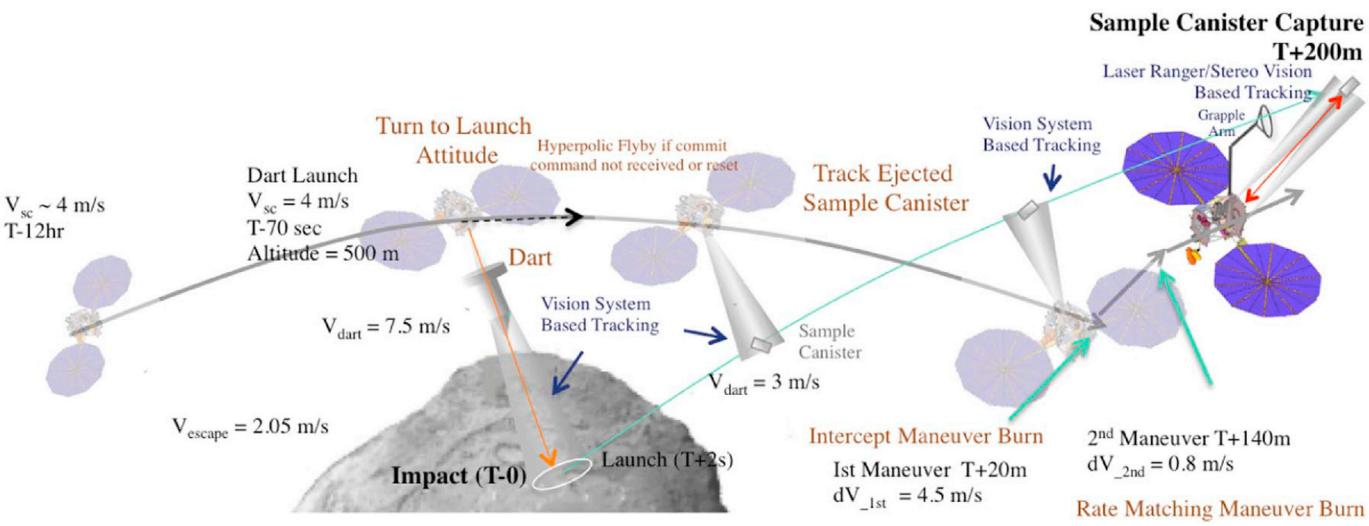

Fig. 3. Mission scenario.

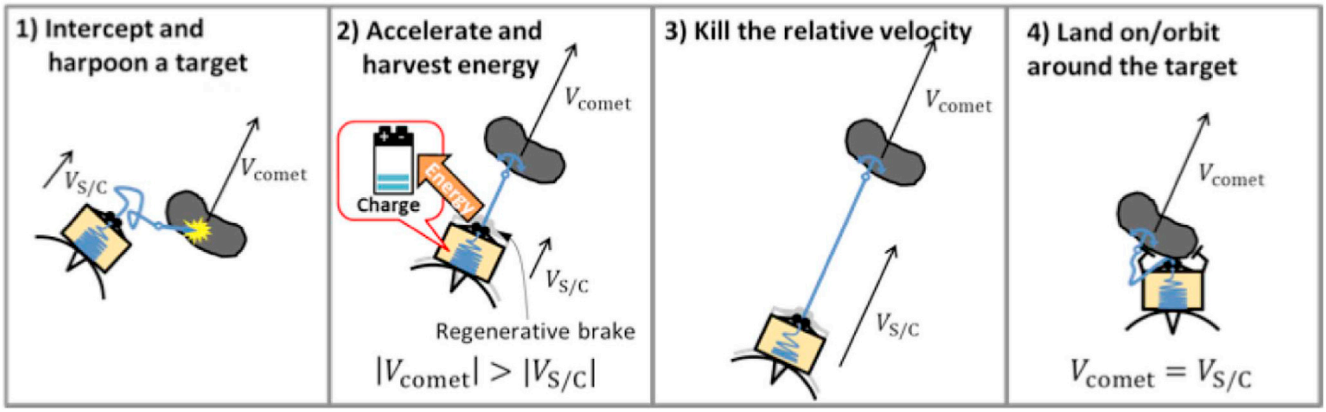

Fig. 4. Space hitchhike maneuver for small body rendezvous and landing.

makes a close flyby in order to attach a tether to the target. Then, as the target moves away, it reels out the tether while applying regenerative brake to give itself a moderate ($<5g$) acceleration. If there is a sufficient length of tether, the spacecraft can eventually make the relative velocity sufficiently small so that it is captured by the weak gravity of the target. At the end of the hitchhike maneuver, the spacecraft is at a significant distance from the target – typically 10–1000 km, depending on the initial relative velocity. However, re-approaching to the target is very easy because the relative velocity has already been killed. The spacecraft can simply retrieve the tether slowly to come closer to the target, and possibly land on it. Fig. 4 shows a sample sequence of a hitchhike maneuver. This idea can be intuitively understood by the analogy of fishing. Imagine a fisherman on a small boat trying to catch a big fish that runs at a high relative speed. Once the fish is on a hook, the experienced fisherman would let the line go while applying a moderate tension on it, instead of holding it tightly. If the line has a sufficient length, the boat can eventually catch up with the fish with moderate acceleration. In addition, by applying regenerative brake, a Comet Hitchhiker can harvest energy from the target body. Assuming 25% efficiency of a regenerative brake, a 2-ton Comet Hitchhiker can produce ~25 GJ of energy, which is sufficient to drive an instrument with 1 kW power consumption over 290 days. If future storage devices can achieve the energy density of gasoline, 25 GJ can be stored in 500 kg of mass, making it a potential energy source in the outer Solar System. Our concept brings important advantages over a related concept of tether-based flyby [22], which uses a fixed length of tether in order to change the direction of the relative velocity like a gravity assist. This concept cannot be used for landing and orbit insertion because it does not reduce the relative speed. The Comet Hitchhiker concept is distinct in that it reels out a tether while applying regenerative brake force to accelerate itself. This approach allows the spacecraft to match its velocity with that of the target, and as a result, enables soft landings and orbit insertion. An inverse hitchhiker maneuver is performed by using the stored energy in order to make a departure from the target. First, when the hitchhiker is on the surface or in orbit, it attaches a tether to the target. Next, it slowly moves away from the target while deploying the tether. Then, it uses the stored energy to quickly retrieve the tether and accelerate itself. Finally, it detaches the tether.

Grappling tether: Finally, as a model of a grappling tether, we consider a tethered system that is capable of being actuated in such a way as to rendezvous and dock with the target body, which could be a piece of orbital debris, or another spacecraft. In this scenario, the spacecraft would first need to detect the target relative to itself, then plan an approach trajectory for the end effector, eject the ATS towards the target, wrap and lock around the target, then apply the necessarily distributed control actuation to retrieve or reposition the target.

This paper is organized as follows. First, we derive the equations of motion of a multibody system with contacts and collisions. Second, we derive the kinematics and kinetics of a space tethered system in orbit. Third, we focus on the tether material constitutive law, allowing for phase-transitioning behavior. Fourth, we describe the interaction of the end-effector at the end of the tether with the contacting surface. Finally, we discuss the application cases, studied with simulation.

2. Modeling of multibody tethered system with contact interactions

In this section, we follow the notation used in [11,3]. Fig. 5 shows the kinematic topology of the multibody chain for a tethered system contacting another body. Body 0 is the free-flying spacecraft. Bodies 1–3 represent the tether. Bodies 4 and 5 represent appendages, such the solar panels hinged at the root via a spring tuned to the first fundamental frequency of oscillation. Body 6 represents the free-flying small body.

In the past two decades, researchers have been developing complementarity based formulations to solve contact and collision dynamics problems. A recent review is given in [19], in which the authors compare and contrast the linear and nonlinear complementarity approaches to solving contact dynamics problems. Complementarity based methods are an alternative to classical penalty based methods that rely on a virtual spring–damper model to apply restoring forces at the point of deepest penetration between two bodies in contact. Penalty methods notoriously suffer from oscillatory effects and become numerically unstable when bodies collide with a high velocity. Small time steps and excessively damped implicit integrators used to counter this make the method slow and computationally expensive. Complementarity based methods, on the other hand, assume that the bodies are truly rigid and compute contact forces at each time step to prevent inter-penetration. Complementarity methods use impulsive dynamics to handle collision and contact interactions. They avoid the small time step and stiffening issues encountered in penalty methods by impulsively stepping over non-smooth events. There are two variants of the complementarity formulation – the linear complementarity problem (LCP) formulation and the nonlinear complementarity problem (NCP) formulation. In the LCP formulation, the dynamics is cast as a linear complementarity problem by discretizing the friction cone using a polyhedral approximation. On the other hand, no such approximations are made in the NCP case leading to an exact modeling of the friction cone.

The state of a mechanical system with n_b rigid bodies in three dimensional space can be represented by the generalized positions $\mathbf{q} = [r_1^T, \epsilon_1^T, \ldots, r_{n_b}^T, \epsilon_{n_b}^T]^T \in \mathbb{R}^{7n_b}$ and their time derivatives $\dot{\mathbf{q}}$, where r_i is the absolute position of the center of mass of the i-th body and the quaternion ϵ_i expresses its rotation. One can also introduce the generalized velocities $\mathbf{v} = [r_1^T, \omega_1^T, \ldots, r_{n_b}^T, \omega_{n_b}^T]^T \in \mathbb{R}^{7n_b}$, directly related to $\dot{\mathbf{q}}$ by means of the linear mapping $\dot{\mathbf{q}} = \mathbf{L}(\mathbf{q})\mathbf{v}$ that transforms each angular velocity (expressed in the local coordinates of the body) into the corresponding quaternion derivative $\dot{\epsilon}_i$ by means of the linear algebra formula $\dot{\epsilon}_i = \frac{1}{2} G(\epsilon_i)\omega_i$, with

$$G(\epsilon_i) = \begin{bmatrix} +\epsilon_1 & +\epsilon_0 & -\epsilon_3 & +\epsilon_2 \\ +\epsilon_2 & +\epsilon_3 & +\epsilon_0 & -\epsilon_1 \\ +\epsilon_3 & -\epsilon_2 & +\epsilon_1 & +\epsilon_0 \end{bmatrix} \tag{1}$$

Mechanical constraints, such as revolute or prismatic joints, can exist between the parts: they translate into algebraic equations that constrain the relative position of pairs of bodies. Assuming that a set of constraints is present in the system, for all $i \in \mathscr{B}$ they lead to the scalar equations $\Psi_i(\mathbf{q}, t) = 0$. To ensure that constraints are not violated in terms of velocities, one must also satisfy the first derivative of the constraint equations, that is $\nabla \Psi_i^T \mathbf{v} + \frac{\partial \Psi_i}{\partial t} = 0$ with the Jacobian matrix $\nabla_q \Phi_i = [\partial \Psi_i / \partial \mathbf{q}]^T$ and $\partial \Phi_i^T = \nabla_{\mathbf{q}} \Psi_i^T \mathbf{L}(\mathbf{q})$. Note that the term $\frac{\partial \Psi_i}{\partial t}$ is zero for all scleronomic constraints, but it might be nonzero for constraints that impose some trajectory or motion law, such as in case of motors and actuators. If contacts between rigid bodies must be taken into consideration, colliding shapes must be defined for each body, and a collision detection algorithm must be used to provide a set of pairs of contact points for bodies whose shapes are near enough, so that a set $\mathscr{A}$ of inequalities can be used to concisely express the non-penetration condition between the volumes of the shapes, i.e. for all $i \in \mathscr{A}$, $\Phi(\mathbf{q}) \geq 0$. Note that for curved convex shapes, such as spheres and ellipsoids, there is a unique pair of contact points, that is the pair of closest points on their surfaces, but in case of faceted or non-convex shapes there might be multiple pairs of contact points, whose definition is not always trivial and whose set may be discontinuous. Given two bodies in contact $\mathscr{A}, \mathscr{B}$, let n_i be the normal at the contact pointing toward the exterior of body $\mathscr{A}$, and let $\mathbf{u}_i$ and $\mathbf{w}_i$ be two vectors in the contact plane such that $\mathbf{n}_i, \mathbf{u}_i, \mathbf{w}_i \in \mathbb{R}^3$ are mutually orthogonal vectors: when a contact i is active, that is for $\Phi(\mathbf{q}) = 0$, the

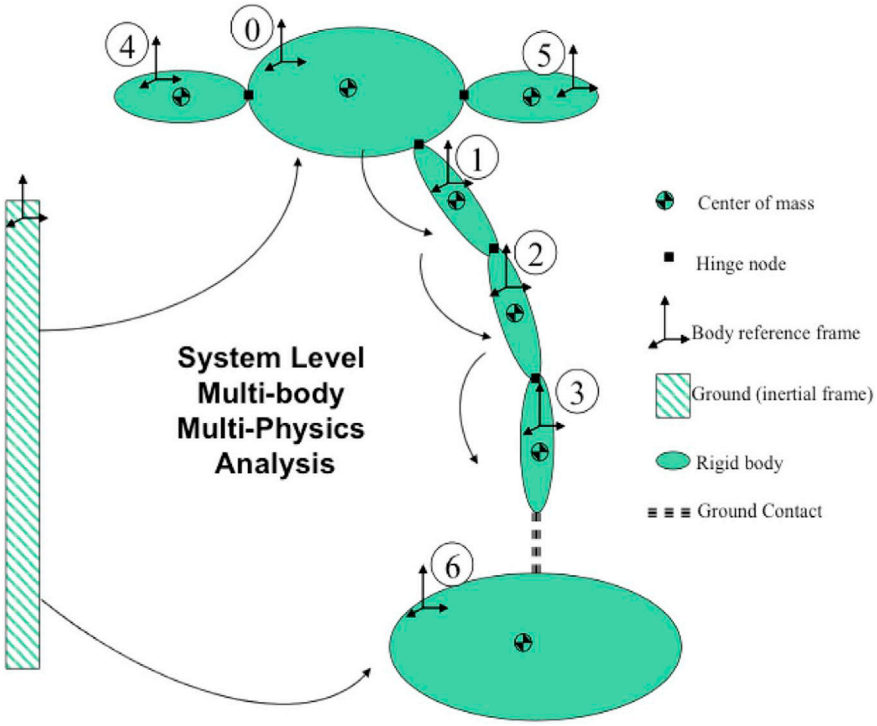

Fig. 5. Multibody dynamics model of contact event with tethered spacecraft system.

frictional contact force acts on the system by means of multipliers $\hat{\gamma}_{i,n} \geq 0$, $\hat{\gamma}_{i,u}$, and $\hat{\gamma}_{i,w}$, that is the normal component of the contact force acting on body $\mathscr{B}$ is $\mathbf{F}_{i,N} = \hat{\gamma}_{i,n}\mathbf{n}_i$ and the tangential component is $\mathbf{F}_{i,T} = \hat{\gamma}_{i,u}\mathbf{u}_i + \hat{\gamma}_{i,w}\mathbf{w}_i$ (for body $\mathscr{B}$ these forces have the opposite sign).

Also, according to the Coulomb friction model, in case of nonzero relative tangential speed $\mathbf{v}_{i,T}$ the direction of the tangential contact force is aligned with $\mathbf{v}_{i,T}$ and it is proportional to the normal force as $\| \mathbf{F}_{i,T} \| = \mu_{i,d} \| \mathbf{F}_{i,N} \|$ by means of the dynamic friction coefficient $\mu_{i,d} \in \mathbb{R}^+$. However, in case of null tangential speed, the strength of the tangential force is limited by the inequality $\| \mathbf{F}_{i,T} \| \leq \mu_{i,s} \| \mathbf{F}_{i,N} \|$ using a static friction coefficient $\mu_{i,s} \in \mathbb{R}^+$, and its direction is one of the infinite tangents to the surface. In our model we assume that $\mu_{i,s}$ and $\mu_{i,d}$ have the same value that we will write μ_i for simplicity, so the above mentioned Coulomb model can be stated succinctly as follows:

$$\hat{\gamma}_{i,n} \geq 0, \quad \Phi_i(\mathbf{q}) \geq 0, \quad \Phi_i(\mathbf{q})\hat{\gamma}_{i,n} = 0 \tag{2}$$

The first condition states that the friction force is always within the friction cone, i.e.

$$\mu_i \hat{\gamma}_{i,n} \geq \sqrt{\hat{\gamma}_{i,u}^2 + \hat{\gamma}_{i,w}^2} \tag{3}$$

The second condition states that the friction force and the velocity between two contacting bodies are collinear and of opposite direction, i.e.:

$$\langle \mathbf{F}_{i,T}, \mathbf{v}_{i,T} \rangle = - \| \mathbf{F}_{i,T} \| \| \mathbf{v}_{i,T} \| \tag{4}$$

The third condition, which captures the stick-slip transition, is:

$$\| \mathbf{v}_{i,T} \| \left(\mu_i \hat{\gamma}_{i,n} - \sqrt{\hat{\gamma}_{i,u}^2 + \hat{\gamma}_{i,w}^2}\right) \tag{5}$$

Note that the condition $\hat{\gamma}_{i,n} \geq 0, \Phi_i(\mathbf{q}) \geq 0, \Phi_i(\mathbf{q})\hat{\gamma}_{i,n} = 0$ can also be written as a complementarity constraint: $\hat{\gamma}_{i,n} \geq 0, \Phi_i(\mathbf{q}) \geq 0$, see [31]. This model can also be interpreted as the Karush–Kuhn–Tucker first order conditions of an equivalent maximum dissipation principle [20], which can be written as:

$$\begin{aligned} &i \in \mathscr{A}: \quad \hat{\gamma}_{i,n} \geq 0, \perp \Phi_i(\mathbf{q}) \\ &\geq 0, (\hat{\gamma}_{i,u}, \hat{\gamma}_{i,w}) \quad \underset{\mu_i \hat{\gamma}_{i,n} \geq \sqrt{\hat{\gamma}_{i,u}^2 + \hat{\gamma}_{i,w}^2}}{\operatorname{argmin}} \mathbf{v}^T(\hat{\gamma}_{i,u}\mathbf{D}_{i,u} + \hat{\gamma}_{i,w}\mathbf{D}_{i,w})) \end{aligned} \tag{6}$$

Finally, we must also consider the effect of external forces with the vector of generalized forces $\mathbf{f}(t, \mathbf{q}, \mathbf{v}) \in \mathbb{R}^{6n_b}$, that might contain gyroscopic terms, gravitational effects, forces exerted by springs or dampers, torques applied by motors, and so on. Considering the effects of both the set $\mathscr{A}$ of frictional contacts and the set $\mathscr{B}$ of bilateral constraints, the system cannot be reduced neither to an ordinary differential equation (ODE) of the type $\dot{\mathbf{v}} = \mathbf{f}(t, \mathbf{q}, \mathbf{v})$ nor to a differential-algebraic equation (DAE), because of the inequalities and because of the complementarity constraints, that rather turn the system into a differential inclusion of the type $\dot{\mathbf{v}} \in \mathscr{F}(t, \mathbf{q}, \mathbf{v})$, where $\mathscr{F}$ is a set-valued multifunction. In fact, the time evolution of the dynamical system is governed by the following differential variational inequality (DVI):

$$\begin{cases} \dot{\mathbf{q}} = \mathbf{L}(\mathbf{q})\mathbf{v} \\ \mathbf{M}\dot{\mathbf{v}} = \mathbf{f}(t, \mathbf{q}, \mathbf{v}) + \sum_{i \in \mathscr{B}} \hat{\gamma}_{i,n} \nabla \Psi_i + \sum_{i \in \mathscr{A}} (\hat{\gamma}_{i,n}\mathbf{D}_{i,n} + \hat{\gamma}_{i,u}\mathbf{D}_{i,u} + \hat{\gamma}_{i,w}\mathbf{D}_{i,w})) \\ i \in \mathscr{B}: \quad \Psi_i(\mathbf{q}, t) = 0 \\ i \in \mathscr{A}: \quad \hat{\gamma}_{i,n} \geq 0, \perp \Phi_i(\mathbf{q}) \geq 0, \\ (\hat{\gamma}_{i,u}, \hat{\gamma}_{i,w}) \quad \underset{\mu_i \hat{\gamma}_{i,n} \geq \sqrt{\hat{\gamma}_{i,u}^2 + \hat{\gamma}_{i,w}^2}}{\operatorname{argmin}} \mathbf{v}^T(\hat{\gamma}_{i,u}\mathbf{D}_{i,u} + \hat{\gamma}_{i,w}\mathbf{D}_{i,w})) \end{cases} \tag{7}$$

Here, to express the contact forces in generalized coordinates, we used the tangent space generators $D_i = [\mathbf{D}_{i,n}, \mathbf{D}_i u, \mathbf{D}_{i,w}] \in \mathbb{R}^{6n_b \times 3}$ that are sparse and are defined given a pair of contacting bodies A and B as:

$$D_i^T = \begin{bmatrix} \mathbf{0} & \dots & -A_{i,p}^T & +A_{i,p}^T A_A \widetilde{\mathbf{s}}_{i,A} & \mathbf{0} & \dots \\ \mathbf{0} & \dots & +A_{i,p}^T & -A_{i,p}^T A_B \widetilde{\mathbf{s}}_{i,B} & \mathbf{0} & \dots \end{bmatrix} \tag{8}$$

where we use $A_{i,p} = [\mathbf{u}_i, \mathbf{v}_i, \mathbf{w}_i]$ as the $\mathbb{R}^{3\times3}$ matrix of the local coordinates of the i-th contact, and introduce the vectors $\bar{\mathbf{s}}_{i,A}$ and $\bar{\mathbf{s}}_{i,B}$ to represent the positions of the contact points expressed in body coordinates. A superscript tilde denotes a skew-symmetric operator. The DVI in (2) can be solved by time-stepping methods: in detail, the discretization requires the solution of a complementarity problem at each time step, and it has been demonstrated that it converges to the solution to the original differential inclusion for $h \to 0$ [31]. Moreover, the differential inclusion can be solved in terms of vector measures: forces can be impulsive and velocities can have discontinuities, thus supporting also the case of impacts and giving a weak solution to otherwise unsolvable situations like in the Painlev paradox [31]. This formulation has been used in the modeling and simulation of anchoring processes in granular media, described in [27].

3. Modeling of tethered system kinematics and kinetics

We follow Fig. 6, and the discussion presented in [25]. The motion of the active tethered system is described with respect to a local vertical–local horizontal (LV–LH) orbiting reference frame $(x, y, z) = F_{ORF}$ of origin O_{ORF} which rotates with mean motion Ω and orbital radius R_0. A general type of orbit can be accommodated in the model, as the orbital geometry at the initial time is defined in terms of its six orbital elements, and the orbital dynamics equation for point O_{ORF} is propagated forward in time under the influence of the gravitational field of the primary (Earth for LEO, Sun for Deep Space applications) and of the Earth as third body perturbation effect. The origin of this frame coincides with the initial position of the center of mass of the system, and the coordinate axes are z along the local vertical, x toward the flight direction, and y in the orbit normal direction. The inertial reference frame $(X, Y, Z) = F_I$ is geocentric inertial for LEO (X points toward the vernal equinox, Z toward the North Pole, and Y completes the right handed reference frame), and heliocentric inertial for other applications. The orbit of the origin of F_{ORF} is defined by the six orbital elements a (semimajor axis), e (eccentricity), i (inclination), Ω_l (longitude of ascending node), ϖ (argument of perigee), ν (true anomaly), and time of passage through perigee. The transformation between F_{ORF} and F_I is given by $F_{ORF} = \mathbf{R}F_I$ with $\mathbf{R} = \mathbf{R}_3(\varpi + \nu)\mathbf{R}_2(i)\mathbf{R}_3(\Omega_l)$ where $R_i(\cdot)$ denotes a rotation matrix of $(\cdot)$ around the direction specified by the subscript. It is useful to refer the translational dynamics of body i to the origin of F_{ORF}. From Fig. 6, the position vector of a generic structural point with respect to O_{ORF} is denoted by ρ_i, and we have $r_i = R_0 + \rho_i$. We define the state vector as $X = (r_E, \dot{r}_E, R_0, \dot{R}_0, \rho_1, \epsilon_1, \dot{\rho}_1, \omega_1, \dots, \rho_i, \epsilon_i, \dot{\rho}_i, \omega_i, \dots, \rho_N, \epsilon_N, \dot{\rho}_N, \omega_N)$ where r_E defines the position of the Earth in inertial space, and ϵ_i and ω_i represent the quaternion and angular velocity vector of the i-th spacecraft with respect to F_I.

The tether is modeled with N point masses connected by massless springs and viscous dampers. Each tether-connected spacecraft is modeled as a rigid body with internal angular momentum distribution, sensors and actuators, and mass/momentum flow representing the effect of the variable length tether.

There are two possibilities to treat tether deployment and retraction with a lumped mass model: either the mass of the masspoints is kept constant (and their number will vary, implying a mass creation and elimination procedure), or the number of masspoints is kept constant (and their masses will vary). The first case, in which the number of masspoints varies, is more complex than the second case, and requires a state vector of varying dimension which needs to be updated during the simulation. This approach may pose significant problems when state vector variables are received from the estimator and sent to the controller. Therefore, our model assumes that the number of masspoints

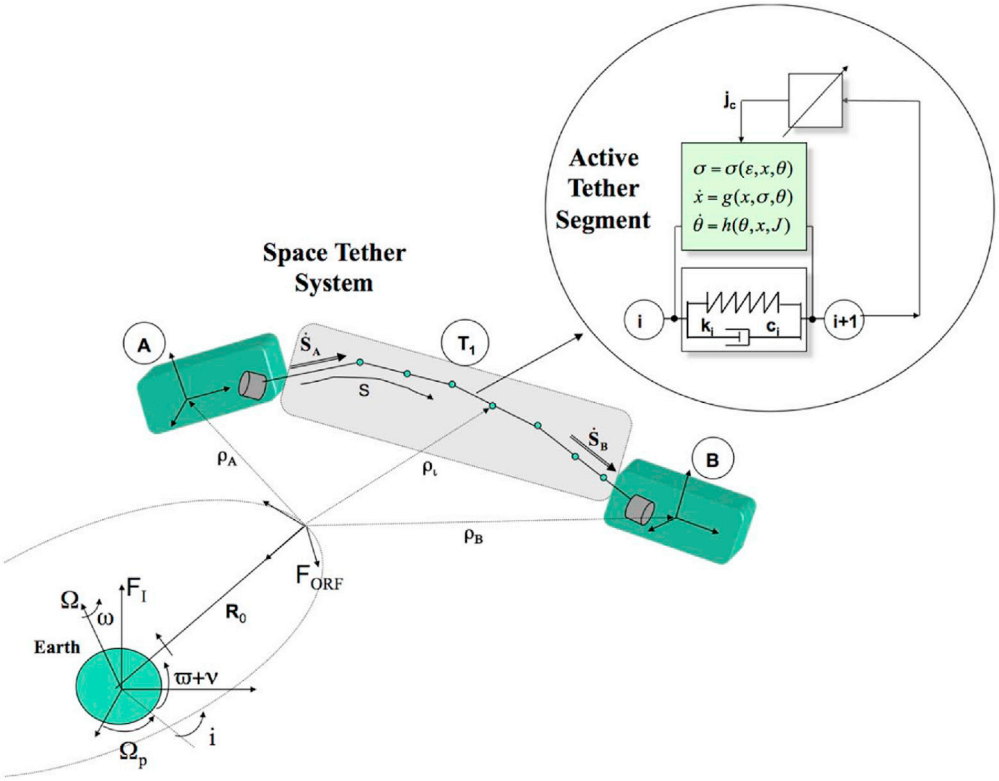

Fig. 6. Model of active tether.

is fixed, and the varying length kinetics is included in the equations by the correct convective terms. A similar analysis is presented in [16], but our derivation is more general and is described in what follows.

Our approach makes use of a material coordinate $\bar{s}$ which describes the arc-length of the tether in the undeformed configuration. Therefore,

$$\frac{d\boldsymbol{\rho}_i}{dt} = \mathbf{v}_i + \frac{1}{\bar{l}\Delta\xi}\left[\frac{d\bar{s}_I}{dt}\tilde{r}(\xi,t) + \frac{d\bar{l}}{dt}\xi\tilde{r}(\xi,t)\right]_{\xi_i}^{\xi_{i+1}} \tag{9}$$

while the dynamic equations may be written as

$$m_i\frac{d\mathbf{v}_i}{dt} = -\dot{m}_i\mathbf{v}_i + \mu\left[\frac{d\bar{s}_{i+1}}{dt}\frac{\partial\rho(\bar{s}_{i+1},t)}{\partial t} - \frac{d\bar{s}_i}{dt}\frac{\partial\rho(\bar{s}_i,t)}{\partial t}\right] - m_i\left[\ddot{\mathbf{R}}_0 + 2\boldsymbol{\Omega}\times\dot{\boldsymbol{\rho}}_i + \boldsymbol{\Omega}\times\boldsymbol{\rho}_i\times\boldsymbol{\rho}_i\right] + \mathbf{f}_i^{grav} + \mathbf{f}_i^{aero} + \mathbf{f}_i^{solar} + \tau_{i+1} - \tau_i \tag{10}$$

considering the tether segment T_i, connecting masses I and J, we have that at time t, $0 \le \bar{s} \le \bar{s}_I(t)$ defines the tether reeled on the I-th spacecraft, $\bar{s}_J(t) \le \bar{s} \le \bar{l}_{total}$ defines the tether reeled on the J-th spacecraft, and $\bar{s}_I(t) \le \bar{s} \le \bar{s}_J(t)$ describes the deployed part of the tether. Clearly, $\bar{s}_I(t)$ and $\bar{s}_J(t)$ are prescribed functions of time representing the deployment and retrieval profiles, and we have that the currently deployed tether length is $\bar{l}(t) = \bar{s}_J(t) - \bar{s}_I(t)$. In F_{ORF}, the position vector of a generic tether point is defined by $\rho(\bar{s},t)$. Capital I and J denote the end masses, while lowercase i denotes tether points.

Let us operate a change of variables such that $\bar{s}(\xi,t) = \bar{s}_I(t) + \xi\,\bar{l}(t)$, so that $\rho(\bar{s},t) = \rho(\bar{s}(\xi,t),t) = \tilde{r}(\xi,t)$. Introducing the tether nodes $\xi_i = \frac{i-1}{N-1}$, i=1,…,N, the tether element is defined by $\xi_i \le \xi \le \xi_{i+1}$. Within this element, the average position $\rho_i(t) = \frac{1}{\Delta\xi}\int_{\xi_i}^{\xi_{i+1}}\tilde{r}(\xi,t)d\xi$ and the mass $m_i(t) = \mu\Delta\bar{s}$, where μ is the tether mass density, represent the position vector and mass of the lumped mass model. After the material differentiation operator, which introduces the convective terms depending on the current tether length and length rate, the kinematic equations of the interior tether points may be written as ($i = 2, \ldots, N-1$)

where $\tilde{r}(\xi_i,t) = \frac{1}{2}(\tilde{r}_{i-1} + \tilde{r}_i)$ and $\frac{\partial\rho(\bar{s}_i,t)}{\partial t} = \frac{1}{2}(v_{i-1} + v_i)$. This is a finite difference approximation of the tether partial differential equation. As such, the large angle tether dynamics is correctly captured, and the approximation improves with the number of tether mass points.

The end body kinematic equations for the I-th spacecraft are

$$\frac{d\boldsymbol{\rho}_I}{dt} = \mathbf{v}_I \tag{11}$$

$$\frac{d\boldsymbol{\epsilon}_I}{dt} = \frac{1}{2}\langle\overline{\omega}_I\rangle\boldsymbol{\epsilon}_I \tag{12}$$

where $\overline{\omega}$ is the augmented angular velocity vector $\overline{\omega} = [\omega^T \quad 0]^T$, and the $\langle\cdot\rangle$ operator performs the quaternion multiplication.

The dynamic equations for the I-th spacecraft are

$$m_I\frac{d\mathbf{v}_I}{dt}=\boldsymbol{\tau}_I-\frac{\mu}{\bar{l}}\left(\frac{d\bar{s}_I}{dt}\right)^2\mathbf{u}_I-m_I\left[\ddot{\mathbf{R}}_0+2\boldsymbol{\Omega}\times\dot{\boldsymbol{\rho}}_I+\boldsymbol{\Omega}\times\boldsymbol{\rho}_I\times\boldsymbol{\rho}_I\right]+\mathbf{f}_I^{grav}+\mathbf{f}_I^{aero}+\mathbf{f}_I^{solar}+\mathbf{f}_I^{control} \tag{13}$$

$$\mathbb{J}_I\frac{d\omega_I}{dt}+\omega_I\times(\mathbb{J}_I\omega_I+\mathbf{h}_I)=\mathbf{g}_I^{ext}+\mathbf{d}_{tether_I}\times\left[\boldsymbol{\tau}_I-\frac{\mu}{\bar{l}}\left(\frac{d\bar{s}_I}{dt}\right)^2\mathbf{u}_I\right]+\mathbf{r}_{cp2cm}\times f_S\frac{\mathbf{r}_I}{|\mathbf{r}_I|^3} \tag{14}$$

$$\dot{\mathbf{h}}_I=-\mathbf{g}_I^{rw} \tag{15}$$

where J_I is the moment of inertia matrix of the I-th spacecraft, h_I represents the total internal angular momentum distribution present in the I-th body (from reaction wheels), and r_{cp2cm} represents the vector from center of mass to center of pressure. Notice the presence of convective terms also in the end mass linear and angular momentum balance equations. They represent the contribution of the momentum flux at the tether feed-out point.

Finally, the tether thermal equilibrium is described by the first order differential equation

$$\dot{\vartheta}=\frac{Q^{solar}+Q^{albedo}+Q^{infrared}-2\pi r\sigma\epsilon\vartheta^4}{\rho cm} \tag{16}$$

where ϑ is the tether temperature, $Q^{[\cdot]}$ represents an input heat flux, r is the tether radius, σ is Boltzmann's constant, ϵ is the tether emissivity, ρ is the tether volume density, c is the tether heat capacity, and m is the tether mass.

Following [26], since the spring mass frequency is too low for the natural material damping to be effective, a longitudinal damper is added in series to the tether itself at one of the tether attachment points. This is a passive damper, tuned to the frequency of the tether bounce mode with a damping ratio of 0.9. An additional dynamic equation is present, representing the linear momentum balance of the tuned damper as

$$k_t l_t=k_d l_d+c_d\dot{l}_d \tag{17}$$

The total tether strain is

$$\varepsilon_{\Delta\xi}=\left[\left(\frac{\bar{l}+l_t+l_d+l_\vartheta}{\bar{l}}\right)-1\right] \tag{18}$$

where l_0 is the tether rest length, l_t is the tether mechanical stretch, l_d is the damper mechanical stretch, and l_ϑ is the tether thermal stretch. The strain rate for the tether segment of length $l_{\Delta\xi}$ is

$$\dot{\varepsilon}_{\Delta\xi}=\frac{\bar{l}\frac{dl_{\Delta\xi}}{dt}-l_{\Delta\xi}\frac{d\bar{l}}{dt}}{(\bar{l})^2} \tag{19}$$

so that the tether tension in the tether segment of length $l_{\Delta\xi}$, stiffness coefficient k and damping coefficient c, is

$$\tau_{\Delta\xi}=k\varepsilon_{\Delta\xi}+c\dot{\varepsilon}_{\Delta\xi} \tag{20}$$

The control laws applied to the spacecraft are of the feedback (proportional-derivative) plus feedforward type. The translation control actually implemented on the spacecraft is of the form

$$\mathbf{f}=\mathbf{K}_p(\mathbf{s}_{Cmd}-\mathbf{s}_{Est})+\mathbf{K}_v(\dot{\mathbf{s}}_{Cmd}-\dot{\mathbf{s}}_{Est})+\mathbf{M}\ddot{\mathbf{s}}_{Cmd} \tag{21}$$

where $\mathbf{s}$ represents the position vector of the center of mass, $\mathbf{K}_p$ and $\mathbf{K}_v$ are translation control gain matrices, $\mathbf{M}$ is the spacecraft mass matrix, $\mathbf{s}_{Est}$ and $\mathbf{s}_{Cmd}$ represent the estimated and commanded translation state, respectively. The rotational control is instead of the following form

$$\boldsymbol{\tau}=\boldsymbol{\Gamma}_p\boldsymbol{\lambda}(\boldsymbol{\theta}_{err})+\boldsymbol{\Gamma}_v(\boldsymbol{\omega}_{Cmd}-\boldsymbol{\omega}_{Est})+\mathbf{J}\ddot{\boldsymbol{\alpha}}_{Cmd} \tag{22}$$

where $\boldsymbol{\Gamma}_p$ and $\boldsymbol{\Gamma}_v$ are rotational control gain matrices, $\mathbf{J}$ is the spacecraft moment of inertia matrix, $\boldsymbol{\lambda}$ is the eigen-axis of rotation, and θ_{err} is the magnitude of rotation corresponding to the difference between the commanded and the estimated quaternions. A feedforward term is used to track a command defined up to an acceleration profile.

4. Modeling of constitutive law of active tether material

The integrated model of the tethered system in which the tether material is an active material is derived in this section. The tether is assumed to act as a generalized spring that undergoes a phase-transition and behaves hysteretically, and the properties of the spring are controllable in a feedback loop. In the model, we also assume that we can measure the position and attitude of the spacecraft, and that we can measure the contact force. Summarizing the above assumptions in analytic form, the physics of the system is described by a structural dynamics equation of motion for the physical displacements q in the second order ODE form

$$M(q)\ddot{q}+C(q,\dot{q})\dot{q}+K(q)q=f(q,\dot{q},\ddot{q}) \tag{23}$$

a phase transition balance equation for the transitioning phases ϕ

$$\dot{\phi}=g(\phi,\sigma,\theta) \tag{24}$$

where σ is the stress on the tether, and θ is the temperature, a thermal balance equation

$$\dot{\theta}=h(\theta,\phi,J) \tag{25}$$

where J is the controlling current, and the set of initial conditions $(q(0)=q_0,\dot{q}(0)=\dot{q}_0,\theta(0)=\theta_0,\phi(0)=\phi_0)$. The actuation inputs are the contact force f, the temperature θ, and the current J. In conclusion, for a given applied stress and Joule heat, we can evaluate the phase fractions and the temperature by integrating the system of equations simultaneously, and then calculate the resulting strain. Alternatively, by prescribing strain and Joule heat, we can compute the phase fractions, temperature, and stress. While the model in this section has been derived with a shape-memory material in mind for simplicity, other active materials would follow the same model electro-strictive, magneto-strictive, photo-strictive, electro-rheological, magneto-rheological, and others, such as electro-active polymers [5].

Fig. 7 shows a block diagram of the adaptive behavior of an active tether. The central block describes the dynamic constitutive laws of the material, as described above. The block at the bottom describes a tether element between two structural nodes. The top block indicates an adaptation mechanism, implemented through feedback of the tether state, in order to apply the adaptive control action.

Past studies [26] with shape-memory materials (SMM) on metallic booms have shown that tip contact force modulation through distributed control of the boom elasticity is possible, provided that thermal equilibrium can be maintained, which in turn dictates the type of smart material to be used. Also, contact force modulation through distributed control of the metallic boom elasticity was shown not only to be possible, but also to cause weak dynamic coupling with the spacecraft, hence modulation of the sample collection dynamics by means of phase-transition control is feasible. Distributed sensing along the boom length, which is needed for buckling control during contact, is feasible by sensing the curvature along the length and feeding back an electric signal at the various stations as the contact forces are monitored, using well-established distributed sensing and control approaches for continuum robots [12,29]. As an example, consider a 500 kg space-craft hovering at 250 m from the surface. To be able to collect 0.5 kg of unconsolidated regolith from the surface of an

asteroid with a 30 kg end effector, 20 N of force at the sampler are needed for a 2 s dwell-time to penetrate the soil. Assuming the tethered system modeled as a 250 m long spring contacting the surface, the spring axial tension needs to increase from 5 mN to 20 N and held at that level for the duration of the sampling event. This implies a material stress increase of 0.25 MPa, which can easily be accomplished by switching the boom material phase at designated locations along the boom, for example, via Joule heating of a shape memory material, or better with electrical activation of electro-active polymers (EAP). EAPs have been proposed as artificial muscles in the space environment because they can induce strains that are as high as two orders of magnitude greater than fragile electroactive ceramics, are superior to shape memory alloys in higher response speed, lower density, and greater resilience, and they can switch phases with mW of power to a maximum stress level of 40 MPa in milliseconds [5]. When the tethered system grasps the surface via a harpoon, drill, some other end-effector, there will be a variable reaction traveling along the tether back at the spacecraft. However, the duration of the contact event can be timed and the tether can be made to change phases before the back-reaction affects the spacecraft adversely. During deployment, at rates of the order of 10 cm/s, the angular momentum of the extended tether might be considerable, and the rotation rate of the parent spacecraft could change substantially during the tether extension and retraction. However, this effect will be predictable and can be controlled with the attitude control system, which will need to be designed for a maximum tether length. The contact loads and spacecraft angular rates for terrain with slope have been shown [26] to be higher than those with flat terrain, and that lateral forces and lateral angular rates are larger for flat terrain but smaller bending stiffness (more compliant member). Also, a comparison of the spacecraft body rates during contact for various lengths under distributed control indicated that there is little effect on the spacecraft attitude rates due to the boom stiffening when control is applied to implement the boom stiffening, since the rates remain well within the maximum acceptable 0.1°/s bound.

5. Modeling of end-effector interactions with a planetary body surface

Modeling and simulation of the harpooning process of asteroidal bodies has been discussed in [4]. In general, slow harpooning methods such as those based on drilling or melters would require the spacecraft Attitude Control System (ACS) to be involved for vehicle stabilization. Conversely, fast harpooning method such as those based on tethered spikes, telescoping spikes, and multi-legged with tethered or telescoping spikes would likely require less ACS involvement. Early studies on harpooning for the ST4/Champollion mission selected a 1 kg 1.9 cm diameter truncated cone penetrator for harpooning onto the surface on materials of strength up to 10 MPa with a 45° impact angle within a reasonable velocity range (100–200 m/s) with a minimum pullout resistance of 450 N in any direction. Several harpooning deployment/retrieval issues must be carefully considered that could impact the mission design. A harpoon may ricochet adversely on surface instead of solidly emplacing on ground. Also, drilling a helical harpoon requires a torque transfer to another object. PHILAEs landing gear uses ice screws and three landing legs with two pods in each, for example. Harpoons could be easily launched before landing. More than one harpoon would need to be deployed from the spacecraft to ensure static stability. Spacecraft ACS (reaction wheels, not RCS) would probably be needed to be on during the harpooning Phase to avoid slack cables and vehicle stability problems. Some harpoon designs would allow them to be pulled out, others would not. Behavior of the regolith is likely governed by cohesion and surface adhesion effects that dominate particle interactions at small scales through van der Waals forces. Electrostatic forces are generally negligible except near terminator crossings where it can lead to significant dust transport. The micro-gravity and solar radiation dominate system behavior prior to soil engagement or penetration. Soil mechanics experiments have known issues when it comes to testing samples of regolith in one-g. First, a reproducible preparation of a homogeneous soil sample is difficult to achieve. Second, a characterization of the soil properties in depth is difficult, since static parameters are typically measured at the surface. Third, under 1-g load, according to soil theory, the compressive strength in depth is significantly influenced by overburden terms, i.e. the effective strength/resistance increase with depth. The soil shear stress can be modeled as $\sigma_c = c + p\tan(\phi_f)$, i.e., the Mohr–Coulomb limit soil bearing capacity theory, where ϕ_f is known as the friction angle (or internal-angle-of-friction), p is the normal pressure, and the zero normal-stress intercept, c, is known as the cohesion (or cohesive strength, i.e. shear stress at p=0) of the soil. For typical regolith simulant, the cohesion is 40 Pa at loosely packed conditions and increases to 10 kPa at 100 relative density. The friction angle also increases monotonically from 25° to 60°. The Rosetta Lander design takes advantage of this effect of greatly increased cohesion by local compression of the cometary regolith under the landing pods during landing. Previous relevant regolith modeling work [6], and [14] covers both low-velocity (approx. 1 m/s) impact of blunt bodies into dust-rich, fluffy cometary materials [6], as well as high-velocity (approx. 10 m/s) impact of sharp projectiles on various types of soil [1,2]. The lower limit of the tensile strength is of the order of 1 kPa whereas the probable upper limit can be taken as 100 kPa. The lower limit of tensile strength corresponds to a compressive strength of $c \geq 7$ kPa. This wide range of soil properties must be captured in simulation, which poses a significant challenge. At very low gravity and vacuum conditions the biggest unknown is the material strength of the surface material. Neither the Deep Impact mission nor other comet observations have provided firm data on the strength of cometary material. Theoretical considerations and laboratory measurements for weakly bound aggregates and the few observational constraints available for comets and cometary meteoroids lead to estimates of the quasi-static tensile (or shear) strength of cometary material in the dm to m range as of the order of 1 kPa, while the compressive strength is estimated to be of the order of 10 kPa.

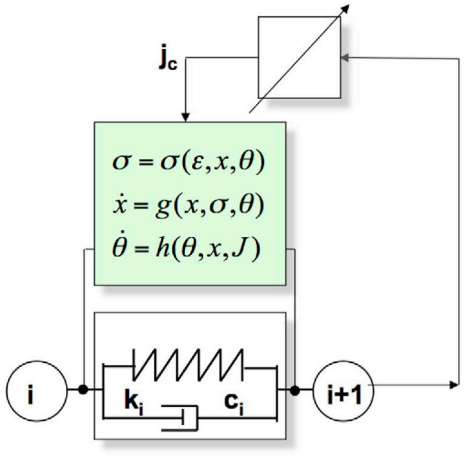

Fig. 7. Adaptive control of active tether.

Now that the foundations of the regolith behavior have been laid out, in the next section we delve into the analysis of the soil interaction process during penetration. A complete and general solution describing the penetration of a projectile into a solid body is not known, though there are several published models available which may be applicable to the harpoon (see, e.g., those listed by Wang [32]). For current modeling efforts we consider the harpoon to be a rigid, conically tipped cylindrical projectile, where θ is the half opening angle of the cone [2]. Several possible forces may contribute to the overall deceleration experienced by the projectile during penetration [1]. These may depend on penetrated depth and velocity as well as target material parameters. Most of the forces can be expressed as the integral of decelerating stresses over the wetted surface S_w of the penetrator in contact with the target material. The main force terms of clear (or plausible) physical origin found in the

published literature are several. First, a constant term associated with compressive strength, possibly including a contribution from the targets' self-weight. The latter should be negligible on the comet, where the surface gravity g is expected to be no more than about 1/2000 of that on Earth. It may be more significant for ground-based experiments where the projectile is fired downwards into a cohesion-less target, though the fact that it is also proportional to the diameter of the projectile means that the term is still quite small for laboratory-scale experiments. Second, a term which increases linearly with depth due to the weight per unit volume ρg of the overlying material (overburden pressure). As with the self-weight, this should be negligible on the small body but needs to be considered for ground-based experiments, especially those with cohesion-less targets. This term is also proportional to a factor $N_q(\phi)$. For the limit $\phi = 0$, N_q=1 and the term becomes analogous to buoyancy in a fluid. Third, a dynamic drag term proportional to the target density ρ and the square of velocity V, resulting from the transfer of momentum from the projectile to the target material. In many cases the importance of drag is incorporated by adopting a drag coefficient C_D (which may itself have a velocity dependence), analogous to the parameter used in fluid dynamics. Fourth, a sliding friction term indicating the friction between the projectile surface and the target material, governed by the coefficient of sliding friction μ_f and the total normal stress from the three terms above. Fifth, a viscosity or damping term, proportional to the component of velocity parallel to the projectiles surface. As with friction, this force acts parallel to the harpoons surface rather than normal to it. The physical validity of this term seems to be a matter for debate. Finally, the weight of the projectile. This is only important when significantly compared to the other (decelerating forces). Collecting these terms together with the appropriate geometric factors, one obtains the following equation for the overall deceleration:

$$-\frac{dV}{dt} = \frac{1}{m}\iint_{S_w}\left[\left(\frac{1}{2}C_D\rho V^2\sin^2\theta\prime + \sigma + \rho g N_q z\right) \times (\sin\theta\prime + \mu_f\cos\theta\prime) + k_v V\cos^2\theta\prime\right] dA - g \tag{26}$$

In this equation, $\theta\prime = \theta$ along the conical tip, but $\theta\prime = 0$ along the cylindrical shaft of the penetrating object. Also, from Komle [14], $N_q(\phi) = \exp(\pi\tan\phi)\tan^2(\frac{\pi}{4}+\frac{\phi}{2})$, and k_v is a constant with units of [N s m^{-3}], i.e., those of viscosity divided by the thickness of a representative boundary layer around the projectile where viscous flow occurs. From [14], a parameter analogous to a drag coefficient can be defined in terms of the material parameters as

$$C_D = \frac{2}{(1-\eta)\cos^2\theta} \times \left[\frac{(1-\eta) + 1/\alpha + \eta/(2-\alpha)}{\eta^{\alpha/2}} - \frac{1}{\alpha} - \frac{1}{2-\alpha}\right] \tag{27}$$

where $\alpha = 3\lambda/(3+2\lambda)$, $\lambda = \tan(\phi)$, ϕ is the angle of internal friction, $\eta = 1 - \frac{\rho_0}{\rho}$ is the volumetric strain, ρ_0 is the bulk density of the target material before penetration. The case $\eta = 0$ implies zero compression.

To get insight into the sensitivity of the system to the various parameters involved, we derived a simple one-dimensional model of the system behavior during penetration in [28]. Fig. 8, taken from [28], depicts the soil bearing stress vs. depth as a function of (a) penetrator mass and (b) cone angle, confirming the fact that a larger diameter harpoon would penetrate less, and that a heavier harpoon would penetrate deeper. All these results assume an initial approach velocity of 1 m/s.

Now that we have insight into the system behavior, we apply these models to various scenarios.

6. Example: small body sampling with phase-transition tether

The objective of the phase-transition tether (PTT) [26] is to investigate the potential that intelligent material actuation has to provide mechanically simple and affordable solutions for delivering assets to a surface and for sample capture and possible return. In the PTT example, we have focused on several intelligent materials, but mostly on a shape memory material. Shape memory materials (SMA) possess an interesting property by which the material remembers its original size or shape and reverts to it at a characteristic phase transformation temperature [7]. By training an SMA wire to remember a given straight or curved shape when heated or cooled down to a given temperature, a long wire with low inherent bending stiffness may be ejected or unreeled from a spacecraft and then transformed into a long thin beam via a controlled material phase transition. Once the phase transition has been induced, the wire exhibits a bending stiffness that did not exist before, and the deployed appendage operates now as a stiff robotic arm. Fig. 2 shows a conceptual view of how artificial manipulator tensioning would occur via an embedded SM wire, and a proposed sequence for sample capture phase. Conversely, when the phase transition reverses, the original state of string behavior dominated by axial tension is recovered and the appendage can be reeled back inside the spacecraft. The transition is almost perfectly reversible and, in principle, many cycles can be performed reliably, which would enable either

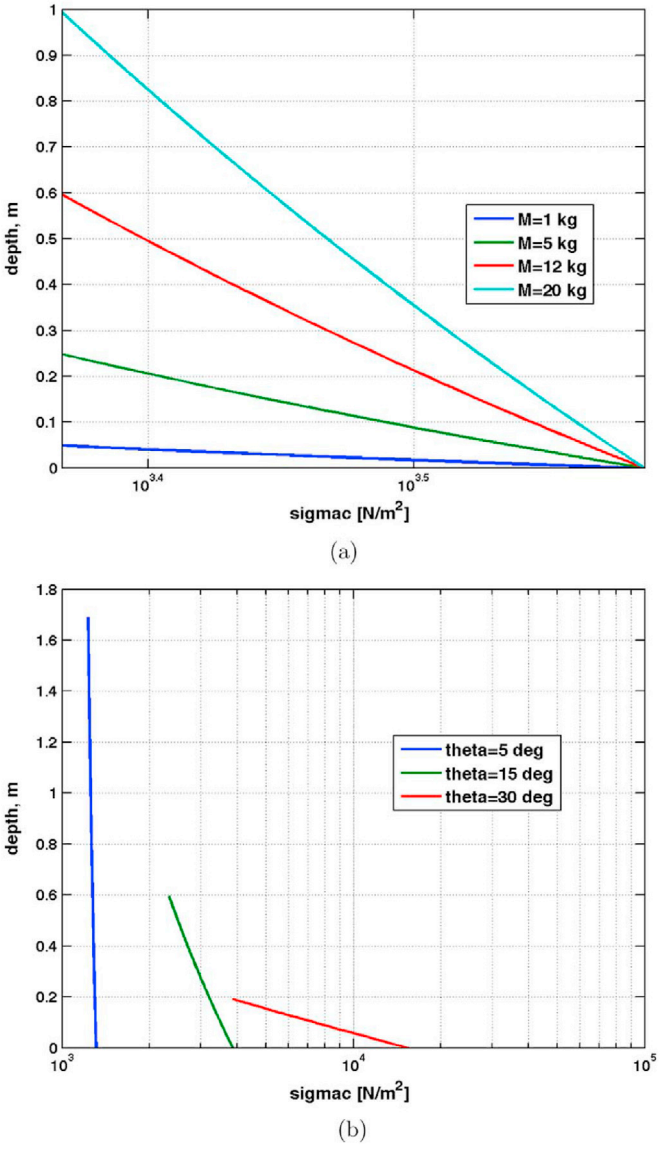

Fig. 8. Soil bearing stress vs. depth as a function of (a) penetrator mass and (b) cone angle.

Property	Value
Range of vertical approach velocity [m/s] along X	[0.1: 0.5]
Range of horizontal approach velocity [m/s] along Y	[-0.1:0.1]
Contact spring stiffness coefficient [N/m]	[1.0:2.0]e4
Contact damper damping coefficient [Ns/m]	[1e1:1e3]
ACS control parameters	Off
Surface slope	[0°:30°]
Surface dynamic friction coefficient	[0.0:1.0]
Duration of contact [s]	[2.0:5.0]
Contact force [N]	[20:30]
SC ascent thrust applied after contact [N]	100
Force sensed by load cell to trigger ascent thruster [N]	5

Fig. 9. Properties of phase-transition simulation.

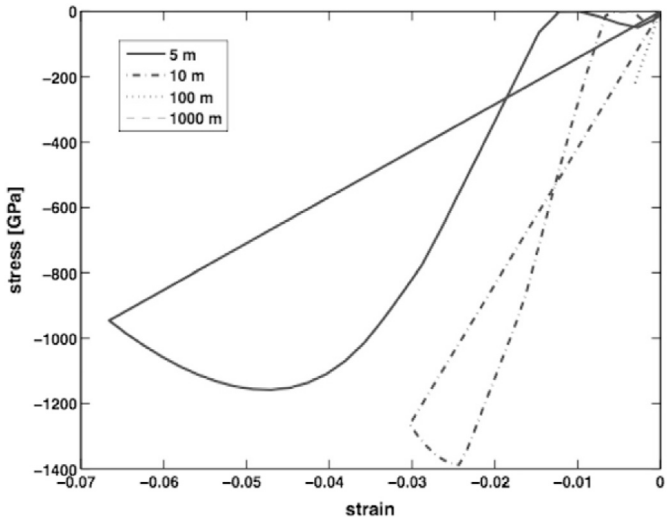

Fig. 10. Stress vs. strain hysteresis curve during contact sampling.

deployment of an asset or retrieval of a collected sample. Shape memory phase transition behavior is tailorable, and compositions exist that have been tested at 99 °C and below. After plastic deformation at low temperature, the SMA returns to its original configuration upon the supply of heat. The material seems to remember its former shape, which gives the name to the effect. At a higher temperature, another important phenomenon can be observed. Here, the material can be reversibly deformed up to 10% of its original length under a nearly constant load this behavior is termed superelasticity. Both effects are a consequence of the load–deformation behavior, which is called quasiplastic at low temperature and pseudoelastic at higher temperature. The underlying mechanism of the observed phenomena is a phase transformation between different crystallographic structures, i.e., different variants of the martensite and the austenite phases. A variety of asset deployment of sample capture scenarios would be possible that could potentially minimize the dynamic interactions with the spacecraft during the maneuver. For example, a minimum load of 20 N was shown to be required to be maintained on the end-effector for approximately 2 *s* so that enough soil sample could be collected from an asteroid, which translated in an adverse reaction on the spacecraft and necessitated additional use of the thrusters to correct the attitude at the end of the maneuver. With the new concept, the stiffness of the end-effector arm can be actively modulated so that the back-reaction on the spacecraft can be greatly reduced. Since the rigidity of the link can now be tailored

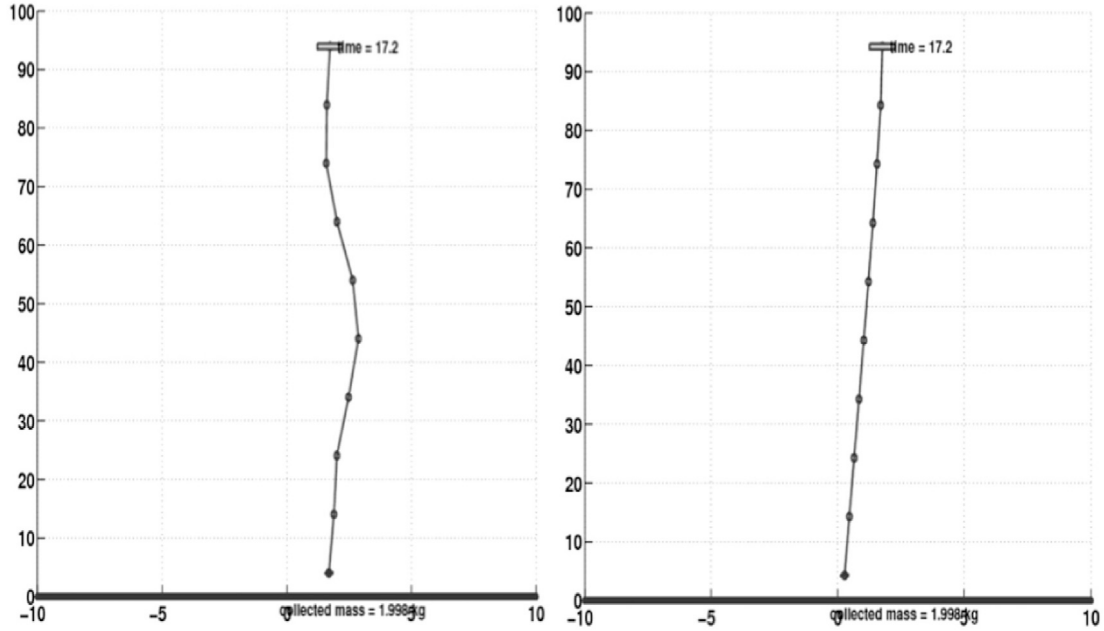

Fig. 11. Comparison of global shape of 100 m boom length without (left) and with (right) distributed phase-transition control.

electrically to specific values, innovative scenarios involving different end-effectors can be envisioned that are highly repeatable, simpler in design, with lower mass, power, and cost. Consequently, we have synthesized the following problem statement: given the spacecraft, manipulator, and terrain models, develop an adaptive control logic and actuator location distribution for the manipulator stiffness that, in conjunction with the attitude and altitude control of the vehicle, decouples the dynamics of the spacecraft from the dynamics of the end-effector while collecting a sample, in a stable manner over a specified amount of time. The adaptive control law is such that the curvature of the manipulator can be modulated over the time the sample has to be collected. To achieve the full potential of shape memory actuation, it is necessary to develop models that characterize the hysteretic nonlinearities inherent in the constituent materials. Additionally, the design of SMA actuators necessitates the development of control algorithms based on those models. We have investigated models that quantify the nonlinearities and hysteresis inherent to phase transition, each in formulations suitable for subsequent control design. Candidate models that have been proposed in the past employ either domain theory to quantify phase transition behavior under isothermal conditions [8,9] or a Muller–Achenbach–Seelecke [23,30] framework, where a transition state theory of non-equilibrium processes is used to derive rate laws for the evolution of material phase fractions. These models involve first-order, nonlinear ordinary differential equations and require few parameters that are readily identifiable from measurements, hence we have selected to use these differential models in our analysis. Shape memory actuators are typically driven by electric current heating. Using the Muller–Achenbach–Seelecke model, for example, the stress–strain constitutive relationship (A=austenite, M=martensite) is given by:

$$\sigma(\epsilon) = \frac{E_M[\epsilon - (x_+ - x_-)\epsilon_0]}{x_+ + x_- + \frac{E_M}{E_A}x_A} \tag{28}$$

The maximum recoverable quasiplastic residual strain ϵ_0 can be identified from experiment. The evolution of the phase fractions x_A, x_+, x_- is governed by the rate laws:

$$\dot{x}_+ = -x_+ p^{+A} + x_A p^{A+}\dot{x}_- = -x_- p^{-A} + x_A p^{A-} \tag{29}$$

where the homogeneity law $X_A + x_+ + x_- = 1$ holds. The quantities in the rates of the phase fractions are transition probabilities, for example, p^{-A} is the transition probability from $M+$ phase to A phase. The transition probabilities are computed as the product of the probability of achieving the energy required to overcome the energy barrier and the frequency at which jumps are tempted. SMA actuators are typically driven by electric current heating. The temperature change coupled with the mechanical loading triggers the phase transformation between martensite and austenite, and generates the material deformation. Assuming that uniform temperature changes through the material, the heat transfer equation becomes:

$$\rho c\dot{\theta}(t) = -\alpha C_v(\theta - \theta_0) - \sigma_R \epsilon_R(\theta^4 - \theta_0^4) + j(t) - (h_{M+} - h_A)\dot{x}_+ - (h_{M-} - h_A)\dot{x}_- \tag{30}$$

where the specific heat c is assumed to be the same for the austenite and martensite phases. The first term is the heat convection to the environment with temperature θ_0. The second term is the heat exchanged with the environment by radiation. The third term is the Joule heating. The last two terms represent the rate dependent heat generation and loss due to the phase transformation, where the h-terms represent the latent heats of transformation of each phase.

Fig. 9, taken from [26], shows the properties used in the simulation of the phase-transition tether. Fig. 10 shows the comparison of the material stress–strain curve during contact for various lengths. Fig. 11 shows a comparison of the global shape of the 100 m boom configuration without (left) and with (right) distributed phase-transition control. The results of these analyses demonstrate that contact force modulation through distributed control of the boom elasticity is not only possible, but also causes weak dynamic coupling with the spacecraft, hence modulation of the sample collection dynamics by means of phase-transition control is feasible. The implementation issues of effective insulation and thermal control during the material phase transition remain to be investigated,

Parameter	Description	Values
M_sc	Spacecraft Mass	2500 kg
l(0)	Launch height (m)	100
M_h	Canister Mass	2 kg
Th	S/C Thrust	[10, 20, 30] N
Vh	S/C horizontal Vel.	@t0=[1, 5, 10] cm/s in +x
Vv	S/C vertical Vel.	@t0=[1, 2, 3] m/s in +y
K	Tether Stiffness	1.1343e+04 N/strain
C	Tether viscoelastic damping	49.24 Ns/strain
dl/dt	Tether retrieval rate	[10, 20, 30] cm/s

Fig. 12. Parameters used in simulation of retrieval of tethered harpoon.

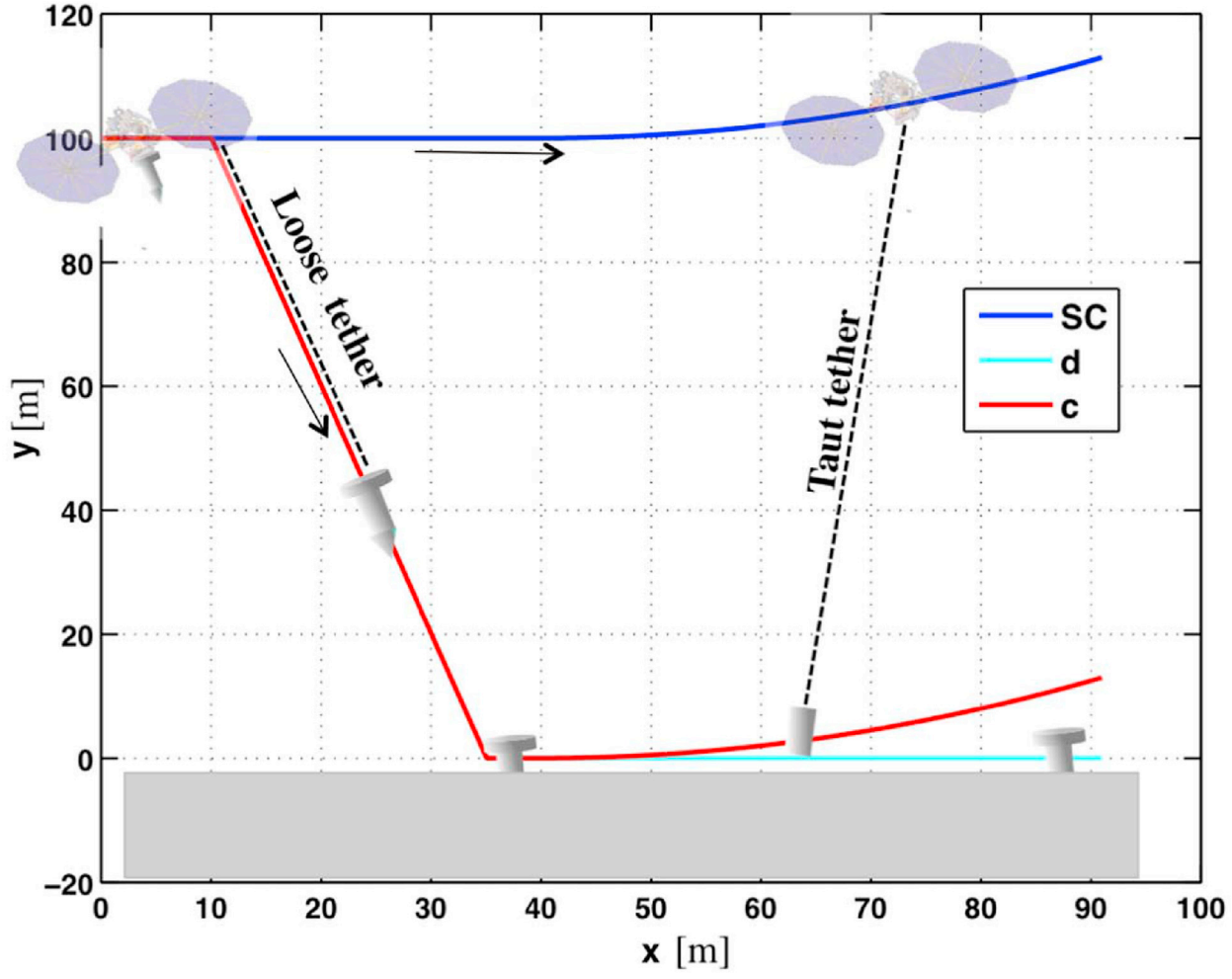

(a)

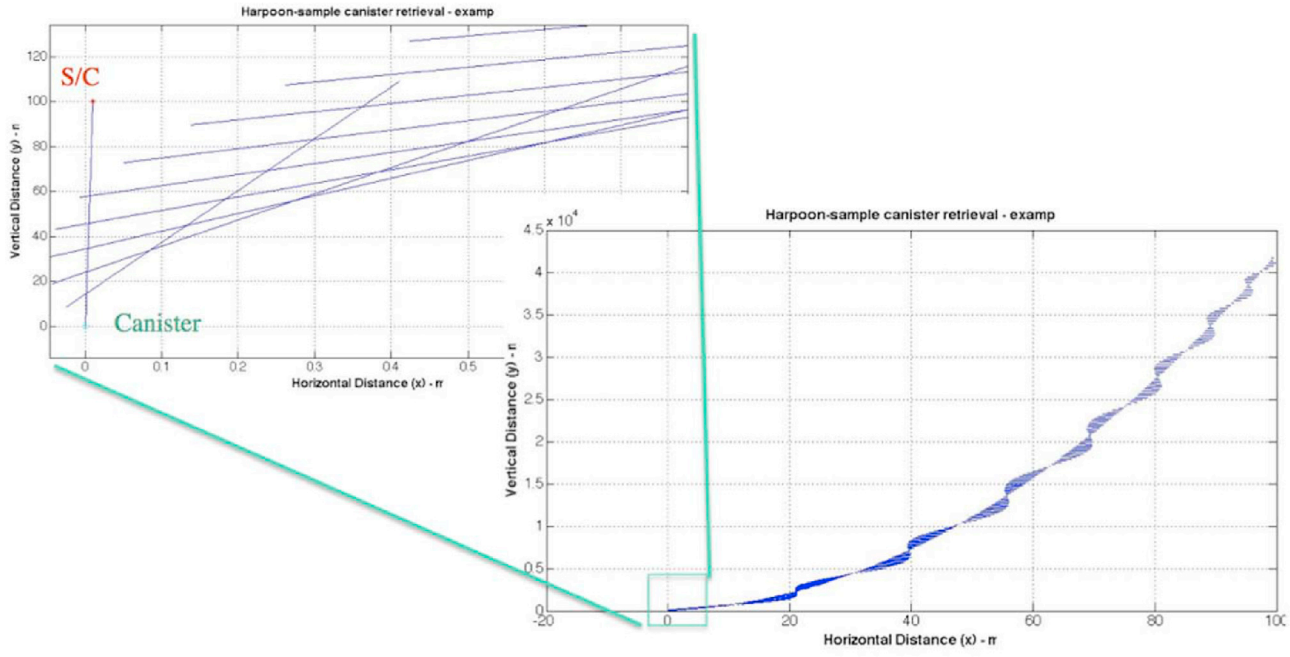

(b)

Fig. 13. (a) Simulation snapshot: with tether and (b) trajectory during tether retrieval.

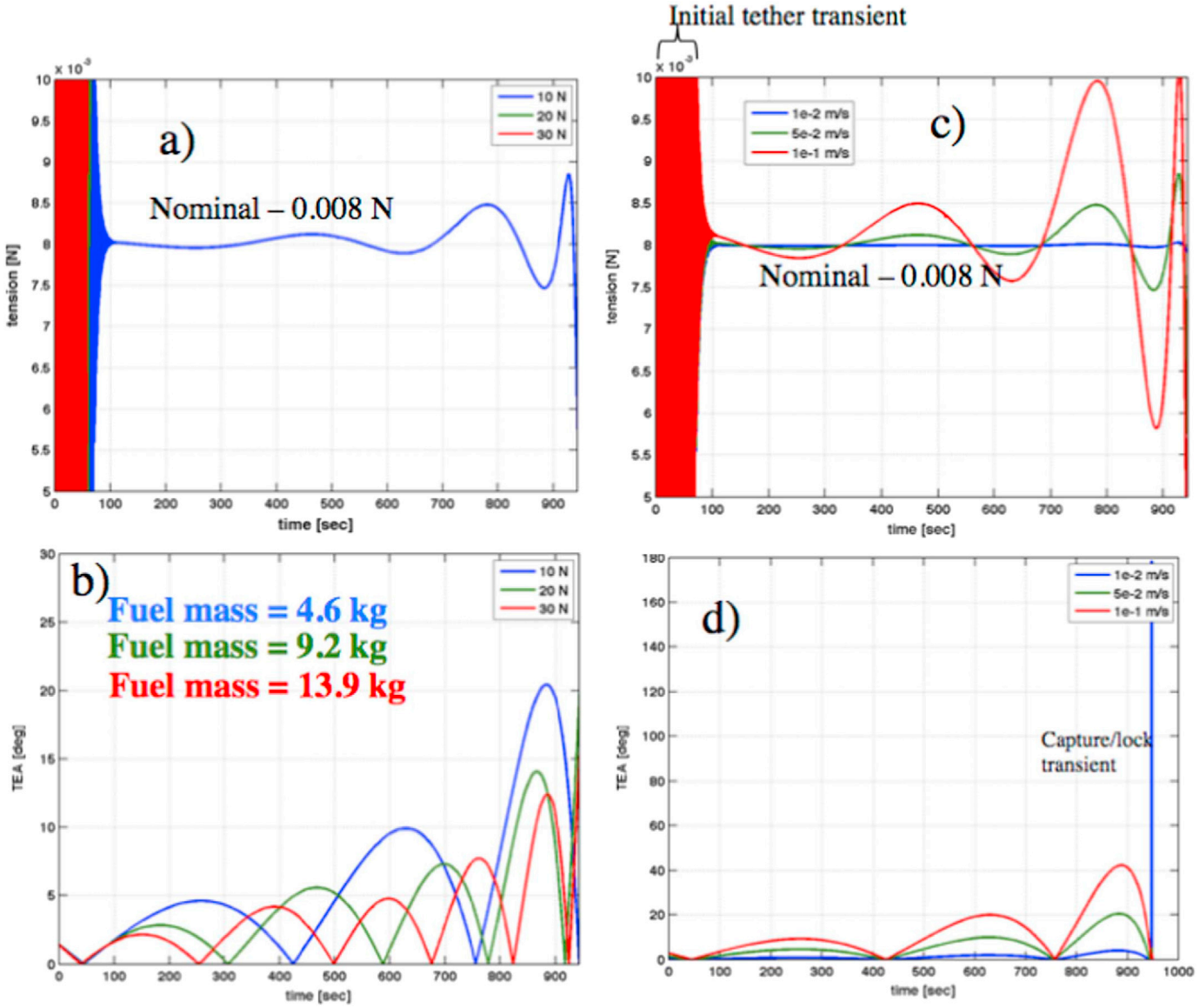

Fig. 14. (a) Tether tension and (b) tether angle varying thrust from 10 to 20 N. (c) Tether tension and (d) tether angle varying the horizontal velocity dispersion from 0.01 to 0.1 m/s.

and will be the subject of future work.

7. Example: tether-assisted retrieval of harpoon during fly-by

In this section, we discuss the effect of adding a tether to retrieve the canister. Fig. 12 summarizes the various system parameters considered in this study. The pictorial depiction of the model and the parameters used in the simulation are shown in Fig. 17(a). A viscoelastic spring–dashpot is used to model the tether, connecting the harpoon to the spacecraft. For simplicity, the problem is two-dimensional. At the initial conditions, the system is hovering along the radial direction, with the canister on the ground at zero velocity (just released from the harpoon casing), while the spacecraft is at 100 m altitude and has velocity initial conditions both in the vertical and in the horizontal directions. These velocity initial conditions represent initial dispersions in velocity accounting for control imperfections. Fig. 17(b) shows the timeline and a snapshot of the tethered harpoon leaving the surface as the spacecraft pulls it. A 0.1 N s ejection impulse from the surface is applied to the canister at 0 s. Spacecraft fly-away acceleration (thrusting) is initiated at 0.2 s, and tether retrieval is initiated after 5 s. The assumed Isp for the spacecraft fly-away thrusters is 220 s.

Fig. 13(b) shows the trajectory of system from initial condition, bringing into evidence the system transfer of angular momentum which takes place the moment the canister is released from the harpoon. The results of the sensitivity study as the fly-away thrust varies from 10 to 30 N and the horizontal velocity dispersion varies from 1 to 10 cm/s are summarized in Fig. 14. These results indicate that the tether retrieval is achievable with reasonable dV fuel budget, and that the tether pendulum model amplitude angle is smaller with larger thrust.

Fig. 14 also shows the sensitivity as a function of increasing the horizontal velocity dispersion from 1 to 10 cm/s, which increases both canister swing angle and tether tension. This case was important to analyze because the canister swing angle was bounded to stay within the camera FOV for visual tracking, especially at close distances.

Fig. 15 shows the sensitivity as the initial vertical dispersion velocity is varied from 1 to 3 m/s and shows that, except for the initial transient, the tether pendulum model amplitude angle is insensitive to vertical velocity dispersion. Fig. 15 also shows the sensitivity as the tether retrieval rate is varied from 10 to 30 cm/s, and shows that the canister angle is sensitive to the tether retrieval rate since, for higher retrieval speeds, a larger tether angle develops sooner, and lead to earlier

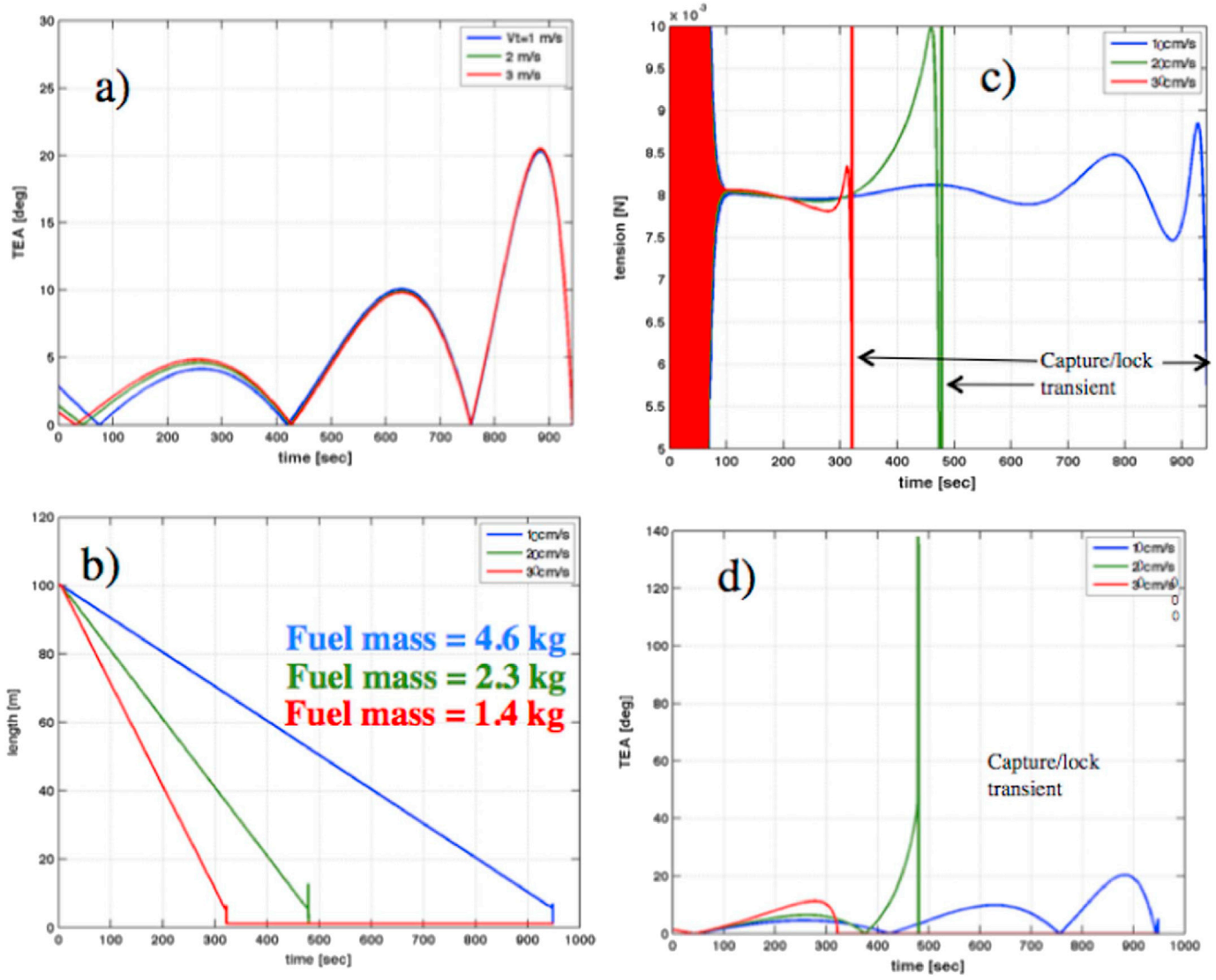

Fig. 15. (a) Tether tension and (b) tether angle varying vertical velocity dispersion from 1 to 3 m/s. (c) Tether tension and (d) tether angle varying tether retrieval speed from 10 to 30 cm/s.

canister capture.

The tether pendulum motion could potentially be reduced with a S/C pendulum cancelation maneuver using well-established techniques of vibration reduction using input shaping. This maneuver would track the canister motion, e.g. visually, and the spacecraft would execute lateral motion to reduce overall tether pendulum angle, repeating the cancelation motion to further reduce pendulum angle.

8. Example: simulation of sling-shot fly-by maneuver

The tether sling-shot gravity assist has already been covered in the literature by various authors [15,22,24]. The analysis of tethered systems with harpoons has also been considered [28]). Consider that the spacecraft has already harpooned to the asteroid. The asteroid gravitational parameter is μ_a and is of radius r_0. The tether connecting the spacecraft to the asteroid is of length L, density ρ and area $A(r)$, to allow for possible tapering. The tether material has Young's modulus E, and tether working strain δ. The spacecraft is rotating about the asteroid at angular rate $\omega = \frac{V_{rel}}{r_0+L}$. The tether tension is $T = \sigma_b A$ where σ_b is the tensile strength of the tether material. The tether longitudinal sound velocity is $C_L = \sqrt{E/\rho}$, the characteristic velocity is $V_c = \sqrt{\sigma/\rho}$, the tether tension along the tether length at station r is $T = \sigma A = m\omega^2 L + \frac{\rho A \omega^2}{2}(L^2 - r^2)$, and the spacecraft-to-tether mass ratio is $m/m_{tether} = (V_c/V_{rel})^2 - 1/2 = \delta(C_L/V_{rel})^2 - 1/2$. This last equation shows that as the spacecraft mass approaches zero, there is an upper limit to the velocity that can be constrained by the tether, namely, $V_{relmax} = \sqrt{2\delta}C_L$. This limit does not depend upon the spacecraft mass or tether length. It is an intrinsic property of the tether material. For Kevlar 49, $C_L = 10$ km/s, and a representative value for the working tether strain is $\delta = 0.01$. (Actually, the breaking strain is $\delta_{max} = 0.02$, therefore, we have an adequate, but not generous, safety factor of 2 in the working strain.) Then, the characteristic velocity is $V_c = \sqrt{\delta}C_L = 1$ km/s, and the maximum spacecraft velocity is $V_{relmax} = 1.4$ km/s. The equation above also places limitations on the achievable relative velocities for a given material and a given spacecraft-to-tether mass ratio M/m. This is shown in Fig. 17(a) for three different materials: Zylon ($E = 5.8$ GPa), Kevlar ($E = 100$ GPa), Carbon Nanotube fiber CNT ($E = 500$ GPa).

The balance of forces of a tether element leads to:

$$\frac{dT}{dr} = \rho A(r)\left(\frac{\mu_a}{r^2} - \omega^2 r\right) \tag{31}$$

(a) Simulation parameters, Zylon case

	Value	Unit
Target		
Center	[0; -30]	km
Semi-axes	[60; 30.1]	km
Spacecraft		
Dry mass	1,000	kg
Initial position	[-100; 10]	km
Initial velocity	[1.67; 0]	km/s
Harpoon		
Mass	10	kg
Ejection velocity	[0; -2.17]	km/s
Tether		
Young's modulus	270	GPa
Density	1560	kg/m^3
Section area	$5.34 \cdot 10^{-6}$	m^2
Available length	120	km
Damping constant	1,000	kNs
Maximum tension (T_{max})	30.97	kN
Simulation		
Step size	0.01	s
Distance between tether point masses	2	km

(b) Simulation parameters, CNT case

	Value	Unit
Target		
Center	[0; -30]	km
Semi-axes	[60; 30.1]	km
Spacecraft		
Dry mass	1,000	kg
Initial position	[-100; 10]	km
Initial velocity	[1.67; 0]	km/s
Harpoon		
Mass	10	kg
Ejection velocity	[0; -2.17]	km/s
Tether		
Young's modulus	270	GPa
Density	1560	kg/m^3
Section area	$5.34 \cdot 10^{-6}$	m^2
Available length	120	km
Damping constant	1,000	kNs
Maximum tension (T_{max})	30.97	kN
Simulation		
Step size	0.01	s
Distance between tether point masses	2	km

Fig. 16. Parameters of hitchhiker simulation (from [21]).

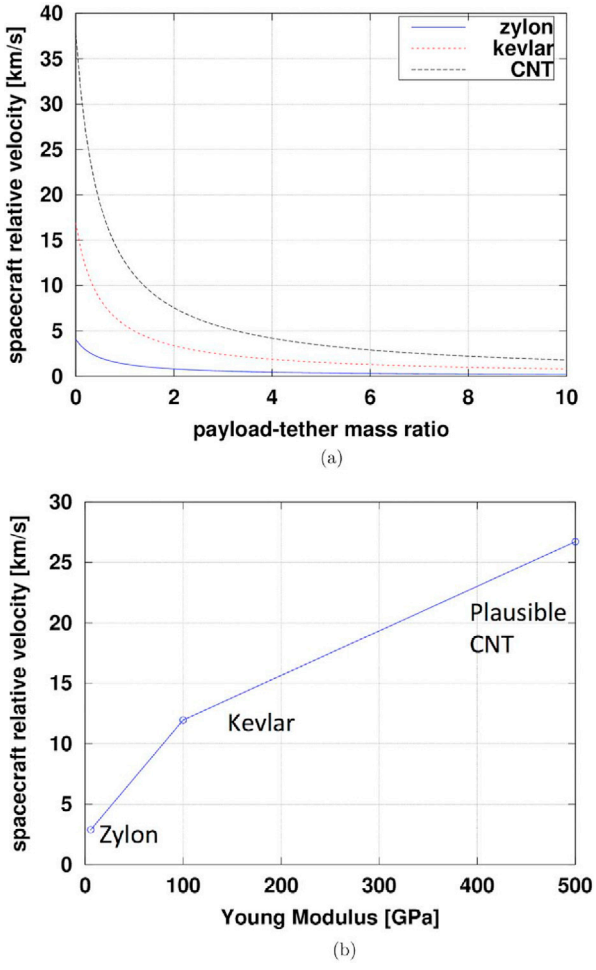

Fig. 17. (a) Velocity limitations for various payload-tether mass ratios and tether strength and (b) maximum ejection velocity as a function of material Young modulus.

In general we should be including asteroid gravity because a massive asteroid may be used for the fly-by, and for a massive asteroid and short tethers it would be comparable to the centrifugal force on the tip mass being ejected. For example, for the proposed Asteroid Redirect Mission, a 1,000,000 kg asteroid of 6 m length, with a spin rate of 2 rpm was considered. Also, tether lengths of 10's of thousandths of kilometers have been considered for this application. However, for now let us neglect asteroid gravity, and include the asteroid spin rate Ω and the angle ϕ between the deployed tether and the normal to the asteroid surface, Ref. [15] arrives at:

$$\frac{dT}{dr} = -\rho A(r)[r(\dot{\phi} + \Omega)^2 + \Omega^2 r_0 \cos\phi] \tag{32}$$

Integrating this equation with $\Omega = 0$, in the constant area case, leads to:

$$T(r,t) = \sigma(r,t)A = L\omega(t)^2\left[m + \frac{\rho AL}{2}\left(1 - \frac{r^2}{L^2}\right)\right] \tag{33}$$

and to

$$T(r,t) = \sigma(r)A(r) = mL\omega(t)^2 \exp\left[\frac{\rho\dot{\phi}_0^2(L^2 - r^2)}{2\sigma_0}\right] \tag{34}$$

in the constant stress case. At r=L, Eq. (34) leads to $v = \sqrt{\frac{2\sigma}{\rho + \frac{2m}{AL}}}$. Assuming m=0, or a very long tether, it becomes $v = \sqrt{\frac{2\sigma}{\rho}}$ Fig. 17(b) shows the ejection velocity as a function of material Young modulus, from the above equation.

In this case of constant area tether, we can write $dT = d\sigma A$, and integrating the balance of forces between the asteroid surface at r_0 and the spacecraft at $r = r_0 + L$, with L being the tether length, we obtain:

$$\sigma(r) = \sigma_0 + \rho\mu_a\left(\frac{1}{r_0} - \frac{1}{r}\right) + \rho\frac{\omega^2}{2}(r_0^2 - r^2) \tag{35}$$

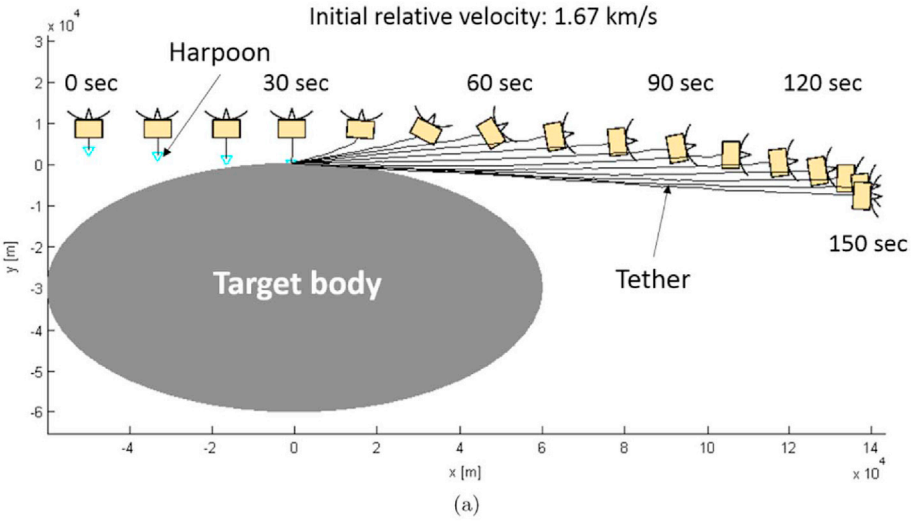

(a)

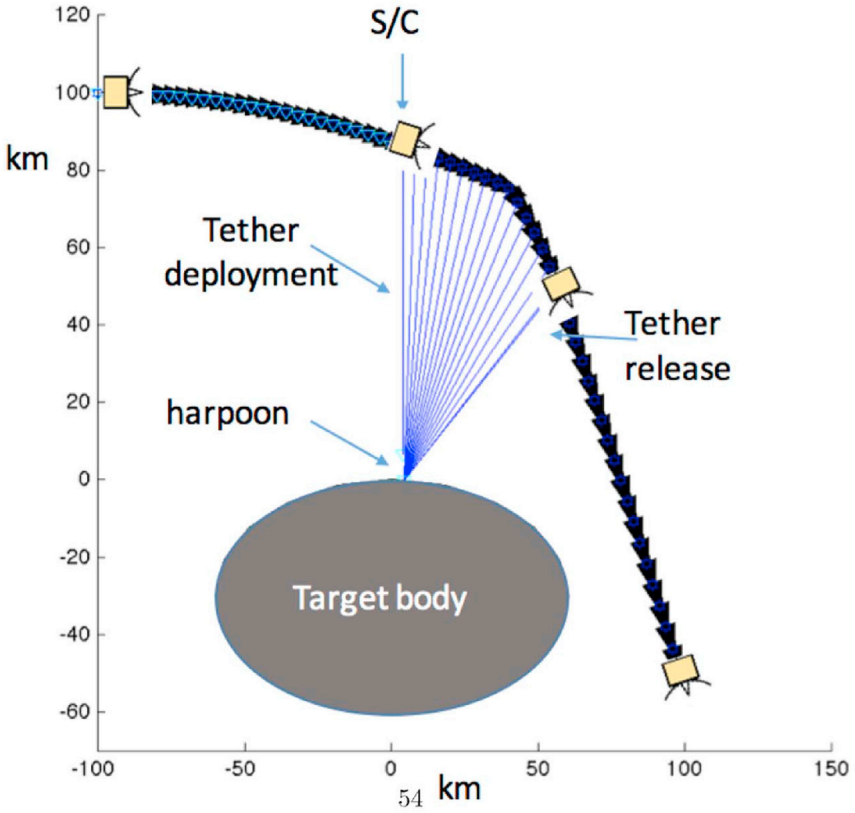

(b)

Fig. 18. (a) A sample sequence of a space hitchhike maneuver (image taken from [21]), and (b) sample sequence of slingshot maneuver with inertial change of direction.

where σ_0 is the stress level at the anchor, equal to the anchoring force, divided by the tether area. This equation shows that there is a maximum distance of $r_{max} = \left(\frac{\mu_a}{\omega^2}\right)^{\frac{1}{3}}$ at which the tether stress reaches the maximum tensile strength. Therefore, a *constant area tether will be limited in length*. For a given tether length L, we can rewrite (36) as:

$$\sigma_{break} = \sigma_0 + \rho\mu_a\left(\frac{1}{r_0} - \frac{1}{r_0 + L}\right) + \rho\frac{V_{rel}^2}{2(r_0 + L)^2}(r_0^2 - (r_0 + L)^2) \tag{36}$$

which gives the attainable V_{rel} for a fixed breaking strength σ_{break} and a fixed tether length L. The total attainable velocity at the end of the fly-by will be $V_{total} = V_{\inf} + V_{rel}$. In case of constant stress tether, we can write $dT = \sigma dA$, and integrating the balance of forces between the asteroid surface at r_0 and the spacecraft at $r = r_0 + L$, with L being the tether length, we obtain:

$$\frac{A(r)}{A_0} = \exp\left\{\frac{\rho}{\sigma}\left(\mu_a\left(\frac{1}{r_0} - \frac{1}{r}\right) + \frac{\omega^2}{2}(r_0^2 - r^2)\right)\right\} \tag{37}$$

where A_0 is the area at the anchor. This equation shows that, at constant stress, the tether will be tapered. A tapered tether *will not break for any tether length, provided the stress is kept less than the breaking strength.*

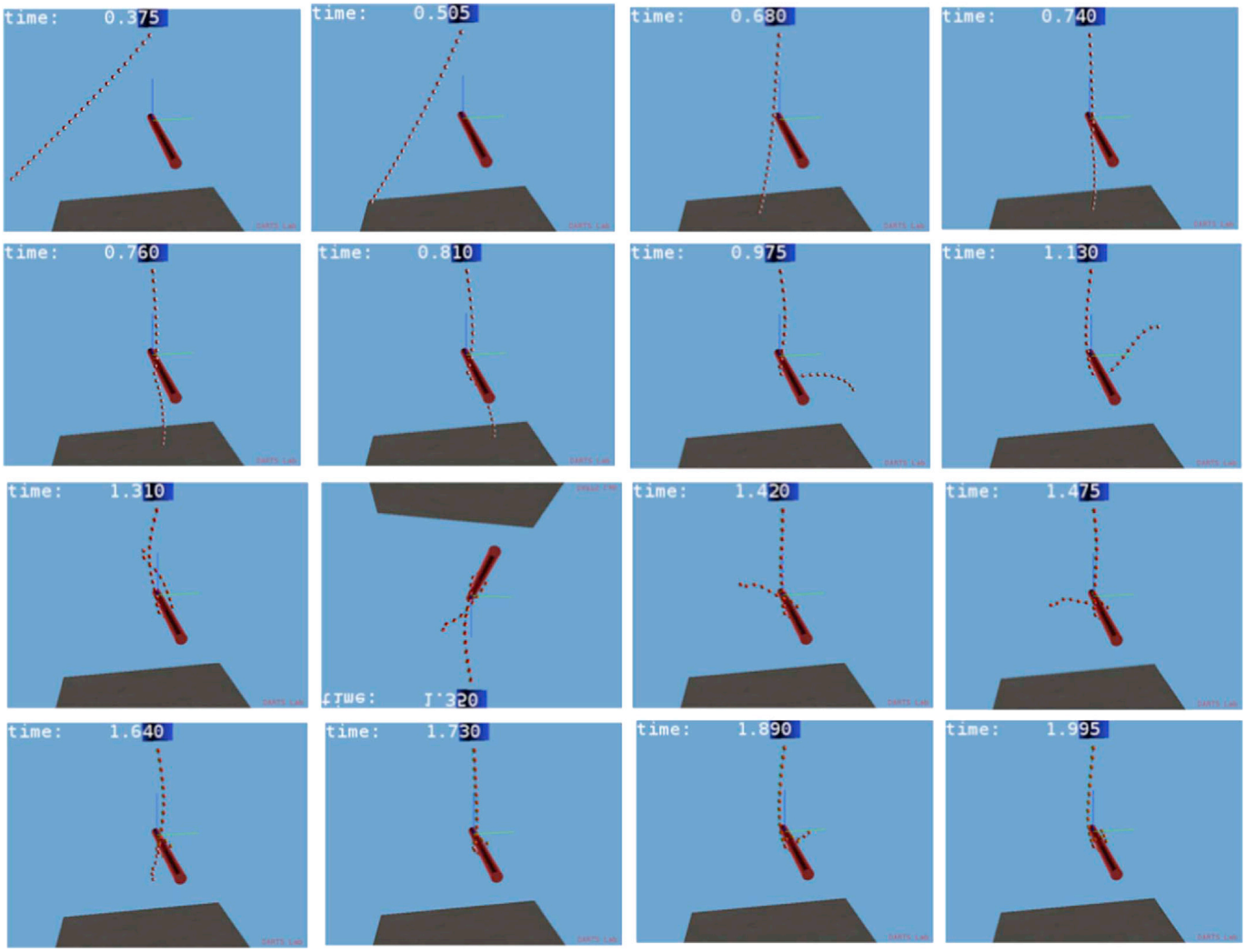

Fig. 19. A sample sequence of the tethered grappling maneuver.

However, it may be very difficult if not impossible to manufacture. For a given tether length L, we can rewrite (37) as:

$$A(r_0+L) = A_0 \exp\left\{ \frac{\rho}{\sigma_{break}} \left(\mu_a \left(\frac{1}{r_0} - \frac{1}{r_0+L} \right) + \frac{V_{rel}^2}{2(r_0+L)^2} \right. \right. \\ \left. \left. (r_0^2 - (r_0+L)^2) \right) \right\} \tag{38}$$

which also gives the attainable V_{rel} for a fixed breaking strength σ_{break}, a fixed tether length L, and a fixed ratio of tether areas $\frac{A(r_0+L)}{A_0}$.

As an example of the tether sling-shot maneuver, the Comet Hitchhiker [21] concept would essentially perform momentum exchange with a target body using an extendable/retrievable tether. Details of the tether finite element simulation are discussed in [21]. In the simulation, we assume that the tension during the sling-shot is controlled in a manner analogous to a fishing reel, which saturates at a certain level of tension. In particular, the amount of deployed tether is held constant as long as the tension felt by the spacecraft is below a certain target tension; above this level, tether is deployed in order to maintain the target level of tension. Fig. 16 shows the parameters used in the simulation. Fig. 18(a) shows a sample sequence of a space hitchhike maneuver simulated by the tether finite element simulator (the size of spacecraft is exaggerated for visualization purposes). Fig. 18(b) shows a sample sequence of a sling-shot maneuver with inertial change of direction.

9. Example: simulation of tether grappling a moving polyhedral object

In this last section, we deal with the simulation of a scenario in which the tether is grappling a moving solid object. This simulation involves the use of a modeling, simulation, and visualization engine for dynamics, such as the one based on the Spatial Operator Algebra [13] used at JPL in the DARTSLab [10]. It also involves non-smooth contact and collision between bodies in motion, which was modeled as a complementarity problem with friction. Fig. 19 shows a sample sequence of the tethered grappling maneuver, in which the tether wraps around the cylindrical spacecraft. This problem was modeled with the complementarity techniques described in [19]. A minimal coordinate operational space formulation is used to model the dynamics of this system. Since minimal coordinates are used, the inter-link constraints are automatically eliminated. No loop-closure bilateral constraints exist for the multi-link tether. Hence, the only constraints acting on the tether system are unilateral contact constraints. The size of the complementarity problem is defined by the number of contacts, which varies as the tether wraps around the target object.

10. Conclusions

This paper has described an approach for modeling, simulation, and control of tethered systems in which the tether is actively controlled. Various aspects of the system model have been described, including tether dynamics, end-effector dynamics, contact interaction and the model of the active tether material. Three scenarios were considered: a tether made of an electrically switchable material for small body sampling, a tether for close-proximity operations such as capture and grappling, and a tether harpooning to a small body for sample capture, fly-by, rendezvous, and/or landing.

The key points that should be taken from this paper are that: (a) Active Tether Systems are a yet undeveloped, but potentially fertile, area of research since they have the potential of exploiting the multi-physics capabilities of intelligent materials with challenging applications requiring tether technology; (b) both quasi-static and highly dynamic space tether mission scenarios offer opportunities for the application of active tethers; and (c) there is synergy and cross-fertilization between recent developments in material science (smart materials) and tether system technology, with great potential for applications in future space missions.

Future work may include higher fidelity modeling and simulations of the Active Tether Systems in the scenarios of operation described in the paper using advanced modeling techniques such as finite elements, or finite differences propagation schemes, as well as experimental tests on prototypes of scaled-down versions of the active tether that would be appropriate for air table testing in a ground laboratory, before conducting further tests in orbit.

Acknowledgment

The research described in this paper was carried out at the Jet Propulsion Laboratory, California Institute of Technology, under a contract with the National Aeronautics and Space Administration. The authors gratefully acknowledge the NASA Innovative Advanced Concepts program for funding support of the Comet Hitchhiker concept (thanks to Dr. Andrew Shapiro-Scharlotta of JPL), and to Dr. Havard Grip of JPL for helping with the Hitchhiker tether simulation.

References

[1] W.A. Allen, E.B. Mayfield, H.L. Morrison, Dynamics of a projectile penetrating sand, J. Appl. Phys. 28 (3) (1957) 370–376.
[2] W.W. Anderson, T.J. Ahrens, A. Gibson, R. Scott, K. Suzuki, Emplacement of penetrators into planetary surfaces, J. Geophys. Res. 101 (E9) (1996) 21,137–21,149.
[3] M. Anitescu, F.A. Potra, D. Stewart, Time-stepping for three-dimensional rigid-body dynamics, Comput. Methods Appl. Mech. Eng. (177) (1999) 183197.
[4] J. Balaram, J. Cameron, A. Jain, H. Kline, C. Lim, H. Mazhar, S. Myint, H. Nayar, R. Patton, M. Pomerantz, M. Quadrelli, P. Shakkotai, K. Tso, Physics-based simulator for NEO exploration: analysis and Modeling, Presented at the AIAA SPACE 2011 Conference and Exposition, Long Beach, California, September 2011, pp. 14–17
[5] Y. Bar-Cohen (Ed.), Electroactive Polymer (EAP) Actuators as Artificial Muscles – Reality, Potential and Challenges, 2nd edition, SPIE Press, Bellingham, Washington, vol. PM136, March 2004, pp. 1–765, ISBN 0-8194-5297-1.
[6] Biele, et al., The putative mechanical strength of comet surface material applied to landing on a comet, Acta Astronaut. 65 (2009) 1168–1178.
[7] V. Birman, Review of mechanics of shape memory alloy structures, Appl. Mech. Rev. 50 (November (11, Pt. 1)) (1997).
[8] J.G. Boyd, D.C. Lagoudas, A. Thermodynamical, Constitutive model for shape memory materials. Part I. The monolithic shape memory alloy, Int. J. Plast. 12 (6) (1996) 805–842.
[9] M.-L. Dano, M.W. Hyer, SMA-induced snap-through of unsymmetric fiber-reinforced composite laminates, Int. J. Solids Struct. 40 (2003) 5949–5972.
[10] Darts Lab Home Page ⟨http://dartslab.jpl.nasa.gov⟩, 2011.
[11] E.J. Haug, Computer-Aided Kinematics and Dynamics of Mechanical Systems, Volume I: Basic Methods, Allyn and Bacon, Needham Heights, Massachusetts, 1989.
[12] M. Ivanescu, D. Cojocaru, N. Bizdoaca, M. Florescu, N. Popescu, D. Popescu, S. Dumitru, Boundary control by boundary observer for hyper-redundant robots, Int. J. Comput. Commun. Control V (5) (2010) 755–767. ISSN 1841-9836, E-ISSN 1841-9844.
[13] A. Jain, Robot and Multibody Dynamics: Analysis and Algorithms, ISBN 978-1-4419-72668-8
[14] N.I. Komle, et al., Impact penetrometry on a comet nucleus interpretation of laboratory data using penetration models, Planet. Space Sci. 49 (2001) 575–598.
[15] E.L. Lanoix, A. Misra, Near-earth asteroid missions using tether sling shot assist, J. Spacecr. Rockets 37 (July–August (4)) (2000) 475–480.
[16] V.V. Beletskii, E. Levin, Dynamics of Space Tether Systems, Advances in the Astronautical Sciences, vol. 83, 1993
[17] S. Matunaga, S. Masumoto, T. Yamanaka, O. Mori, K. Nakaya, Retrieving dynamics and control of tethered sampling method for minor body exploration, Paper AIAA 2006-6763, Presented at AIAA/AAS Astrodynamics Specialist Conference and Exhibit, Keystone, Colorado, 21–24 August 2006.
[18] S. Matunaga, T. Yamanaka, H. Ashida, J. Nishida, K. Nakaya, O. Mori, Microgravity experiment of reel mechanism for tethered sampling, Space Utiliz. Res. 23 (2007).
[19] H. Mylapilli, A. Jain, Evaluation of complementarity techniques for minimal coordinate contact dynamics, in: Proceedings of the ASME 2014 International Design Engineering Technical Conference (IDETC), Buffalo, NY, August, 2014.
[20] J.J. Moreau, Standard inelastic shocks and the dynamics of unilateral constraints, in: G.D. Piero, F. Macieri (Eds.), Unilateral Problems in Structural Analysis, CISM Courses and Lectures no. 288, Springer-Verlag, New York, 1983, pp. 173–221.
[21] M. Ono, M. Quadrelli, G. Lantoine, P. Backes, A. Lopez-Ortega, H. Grip, C. Yen, D. Jewitt, The Hitchhiker's guide to the outer solar system, in: AIAA SPACE 2015, (AIAA 2015-4567), http://dx.doi.org/10.2514/6.2015-4567
[22] P. Penzo, H. Mayer, Tethers and asteroids for artificial gravity assist in the solar system, J. Spacecr. 23 (January–February (1)) (1986) 79–82.
[23] A. Peffer, E. Fosness, B. Carpenter, K. Denoyer, On-orbit experiments and applications of shape memory alloy mechanisms, in: Jack H. Jacobs (Ed.), Smart Structures and Materials 2000: Industrial and Commercial Applications of Smart Structures, Proceedings of SPIE, vol. 3991, 2000.
[24] J. Puig-Suari, J.M. Longuski, S.G. Tragesser, A. Tether, Sling for lunar and interplanetary exploration, Acta Astronaut. 36 (6) (1995) 291–295.
[25] M. Quadrelli, Modeling and dynamics analysis of tethered formations for space interferometry, Presented at the AAS/AIAA Spaceflight Mechanics Meeting, Santa Barbara, CA, Advances in the Astronautical Sciences, vol. 108, February 11–14, 2001, pp. 1259–1278.
[26] B.M. Quadrelli, P. Backes, W.K. Wilkie, J. Keim, U. Quijano, R. Mukherjee, D. Scharf, S.C. Bradford, M. McKee, Investigation of phase transition-based tethered systems for small body sample capture, Acta Astronaut. 68 (2011) 947–973.
[27] M. Quadrelli, H. Mazhar, D. Negrut, Modeling and simulation of harpooning processes for small body exploration, AIAA SPACE 2012 paper AIAA2012-5310, 2012.
[28] M.B. Quadrelli, Modeling and simulation of a tethered harpoon for comet sampling (AIAA 2014-4122), in: AIAA/AAS Astrodynamics Specialist Conference, 2014, http://dx.doi.org/10.2514/6.2014-4122
[29] D.C. Rucker, The mechanics of continuum robots (Ph.D. thesis), Vanderbilt University, 2011.
[30] S. Seelecke, I. Muller, Shape memory alloy actuators in smart structures: modeling and simulation, Appl. Mech. Rev. 57 (January (1)) (2004).
[31] D.E. Stewart, J.C. Trinkle, An implicit time-stepping scheme for rigid-body dynamics with inelastic collisions and Coulomb friction, Int. J. Numer. Methods Eng. 39 (1996) 2673–2691.
[32] W.L. Wang, Low velocity projectile penetration, J. Soil Mech. Found. Div. Proc. Am. Soc. Civ. Eng. 97 (SM12) (1971) 1635–1655.